Bidimensional spectroscopy of double galaxies

II. Mkn 789, UGC 4085, UGC 3995[*]

Eleni T. Chatzichristou[1]**, Christian Vanderriest**[2]**, and Matthew Lehnert**[1]

[1] Sterrewacht Leiden, Postbus 9513, 2300 RA Leiden, The Netherlands
[2] DAEC, Observatoire de Paris-Meudon, 5 Place Jules Janssen, F-92195 Meudon Principal Cedex, France

Abstract. We present data obtained using the integral field spectrograph, SILFID, on the CFHT for three galaxies: Mkn 789, UGC 4085, UGC 3995. These systems are part of a larger ensemble of interacting/merger candidates, that were specifically chosen to have a range of nuclear activity, IR properties and strength of interaction. Unlike slit spectra, these data arrays provide a direct two-dimensional picture of the wavelength-dependent emission and absorption line properties of the galaxies. With the complement of optical photometry, we analyze for each object the kinematics of the gas component and the details of the ionization structure.

Mkn 789 is a recent merger with a fuzzy appearance whose infrared properties make it directly comparable to the powerful FIRGs. It is undergoing large scale star formation that powers a superwind seen as double peaked emission line profiles.

We do not find any evidence for UGC 4085 to be a merger, as the two central knots are elongated, showing typical HII region like spectra and the general velocity field indicates a smooth retrogradely rotating disk.

UGC 3995 is member of a closely interacting pair of galaxies that shows extended "cone"-like ionized gas morphology along a bar-like structure. Additional velocity components detected in the $[OIII]$ profiles are interpreted as gas inflow along the bar, that may be responsible for activating the Seyfert nucleus. On the basis of these data we argue that the gas dynamics in the central (10-20 kpc) regions is dominated by the more energetic hydrodynamic processes rather than directly related to the merger itself.

Key words: galaxies: interactions – galaxies: Seyfert – galaxies: kinematics and dynamics – galaxies: individual: Mkn 789, UGC 4085, UGC 3995

1. Introduction

The link between galaxy merging/interactions and the initiation of galaxy activity has a rich legacy in contemporary theoretical astrophysics. Merging and interactions appear to be an efficient process for transferring large amounts of molecular and gaseous material from galactic scales down to kpc or even pc scales (e.g., Mihos & Hernquist 1996, Barnes & Hernquist 1996 and references therein). Since galaxy interactions potentially operate on a wide range of spatial and temporal scales and with different intensity levels, they can explain the initiation of diverse phenomena ranging from starbursts to non-thermal AGN activity. Theoretical calculations and numerical modeling have shown that strong gravitational interactions between disk galaxies can lead to orbital decay and subsequent merging while, on a dynamical time scale, driving large amounts of interstellar material down to nuclear size scales. Eventual merging of the interacting galaxies can trigger Seyfert activity through the fueling or creation of a central supermassive black hole. Violent star formation may also occur. The time scale for this sequence of events is of the order of a few 10^7 to 10^8 years (e.g., Mihos & Hernquist 1994). The remaining gas might be blown away by supernova- or AGN-driven winds (Lehnert & Heckman 1996). After a billion years or so, the result of this merger may be a remnant with the optical and kinematic signatures of an elliptical galaxy (e.g., Schweizer 1996; Heyl et al. 1996 and references therein) or perhaps even a late type galaxy (Hibbard & van Gorkom 1996).

However, as convincing as the evidence seems for mergers and interactions initiating starburst and perhaps AGN activity, such evidence is circumstantial or qualitative. There are very few studies of the actual dynamical and excitation state of the gas and stars in interacting or merging galaxies. Such information is essential for studying the physical processes that can drive large quantities of gas into the nuclei of galaxies. In order to study the ionized gas distribution and kinematics in merger/interacting candidates, we have begun a program for collecting data using "integral field spectrographs" (in their various incarnations) at the CFHT. This provides detailed information about the emis-

---

Table 1. Observing Log

Object	Date(UT)	Filters Spectral Range	Exposure time (sec)	Field size (arcsec)^2	Spatial sampling	Seeing (arcsec)
Mkn 789	03 March 1992	B	600	$(364)^2$	$0.178''$/pix	1.3
		V	300	$(364)^2$	$0.178''$/pix	1.2
		R	300	$(364)^2$	$0.178''$/pix	1.0
		4200-6900 Å	1800	$(16)^2$	$0.7''$/fibre	1.0
UGC 4085	29 February 1992	B	600	$(364)^2$	$0.178''$/pix	0.8
(I231)		V	480	$(364)^2$	$0.178''$/pix	0.8
		R	300	$(364)^2$	$0.178''$/pix	1.0
		4200-6900 Å	2x2400	$(16)^2$	$0.7''$/fibre	0.8
		5500-8300 Å	2x1800	$(16)^2$	$0.7''$/fibre	0.8
UGC 3995	28 February 1992	B	600	$(364)^2$	$0.178''$/pix	1.2
(I226)		V	300	$(364)^2$	$0.178''$/pix	1.2
		R	300	$(364)^2$	$0.178''$/pix	0.9
		4200-6900 Å	2x1800	$(32)^2$	$1.4''$/fibre	0.8
		5500-8300 Å	2x1800	$(32)^2$	$1.4''$/fibre	0.8

The numbers preceded by an "I" refer to the "Warm IRAS Sources" list of De Grijp et al. (1987).

sion and absorption line properties in three dimensions. In addition, we have obtained some imaging data as a complementary tool to trace the distribution of old stars (R band) and star forming regions (colour maps) and to allow a comparison of these distributions with that of the reconstructed emission line images. We hoped that studying the detailed kinematic and morphological properties of a few Seyfert and starburst galaxies which are undergoing merging would provide clues as to whether there is an evolutionary connection between starburst and AGN/QSO activities. Our data map the ionized gas in the central few kpc region, in the hope of identifying signatures of gas motions tidally induced or associated with the nuclear activity, such as line splitting or distorted rotation curves. Moreover, the search of a relationship between the kinematics and physical conditions in the emitting regions helps to understand what the energy input mechanisms are and to relate them to the galaxy's nuclear activity.

Our sample galaxies were chosen on the basis of several criteria. First, they are infrared-selected (using IRAS data): all are luminous IR sources and were chosen specifically to have a range of IR colour temperatures to represent different dust heating mechanisms. Second, they were chosen to include both types of nuclear activity, starburst and Seyfert. Third, they are all relatively nearby objects, so as to provide good spatial resolution for a detailed mapping of the emission and absorption line properties. Fourth, adopting the evolutionary sequence of galactic merging as proposed by Toomre (1977; which has been further elaborated by Hibbard and van Gorkom 1996), we have chosen objects that appear to be "representative" of various interaction stages. Although these systems by no means represent the full range of the merger sequence, we hope that they can still provide important clues on the effects of the interaction strength on the galaxy structure and on the evolution of these effects with time.

In Chatzichristou & Vanderriest (1995, hereafter Paper I), we have published data for the first object in our sample, Mkn

463 and here we will present similar data for three more objects: Mkn 789, UGC 4085 and UGC 3995.

The present paper is organized in the following way: in Sect. 2 we give an overview of the observations and the techniques used for the data reduction. In Sects. 3, 4 and 5 we present the data and discuss each individual system. Each section is structured in three parts: (i) morphological description and photometric measures, based on direct imaging observations, (ii) distribution of emitting gas in various wavelengths and global characterization of the line profiles and (iii) kinematic analysis vs ionization structure throughout the object. In Sect. 6 we discuss the IR and optical properties combining the results presented in this paper together with the results from Paper I. Finally, in Sect. 7 we give a summary of the main results and in Sect. 8 we outline the future directions of work.

2. Observations, data reduction and analysis

The observations consist of bidimensional spectra and B,V,R images collected at the CFH telescope in February/March 1992, using SILFID (Spectrographe Intégral à Linéarisation par Fibres de l'Image Directe) (for a detailed description of the instrument and the advantages of the technique, see Vanderriest & Lemonnier 1988, Vanderriest 1993 and Paper I). The detector was a 2048×2048 Lick2 CCD with 15 μm pixels ($0.178''$ on the sky).

Each galaxy was observed in the ARGUS configuration designed for integral field spectroscopy. The entrance field consists of 397 fibres (with 100 μm diameter and 4μm cladding), arranged in a compact hexagonal array. We used two grisms giving useful spectral ranges 4400-6800 Å and 5500-8000 Å and 100 Å/mm dispersion. The resolution is slightly better than 5 Å at the center of the field. The field size and spatial sampling depend on the configuration used (direct focus, focal reducer or enlarging lens) and are listed in Table 1 for each object.

In addition, we used the imaging mode of the instrument, to obtain B, V and R direct images for each galaxy. Here the field of view is much larger ($6' \times 6'$) with $0.178''$/pix resolution.
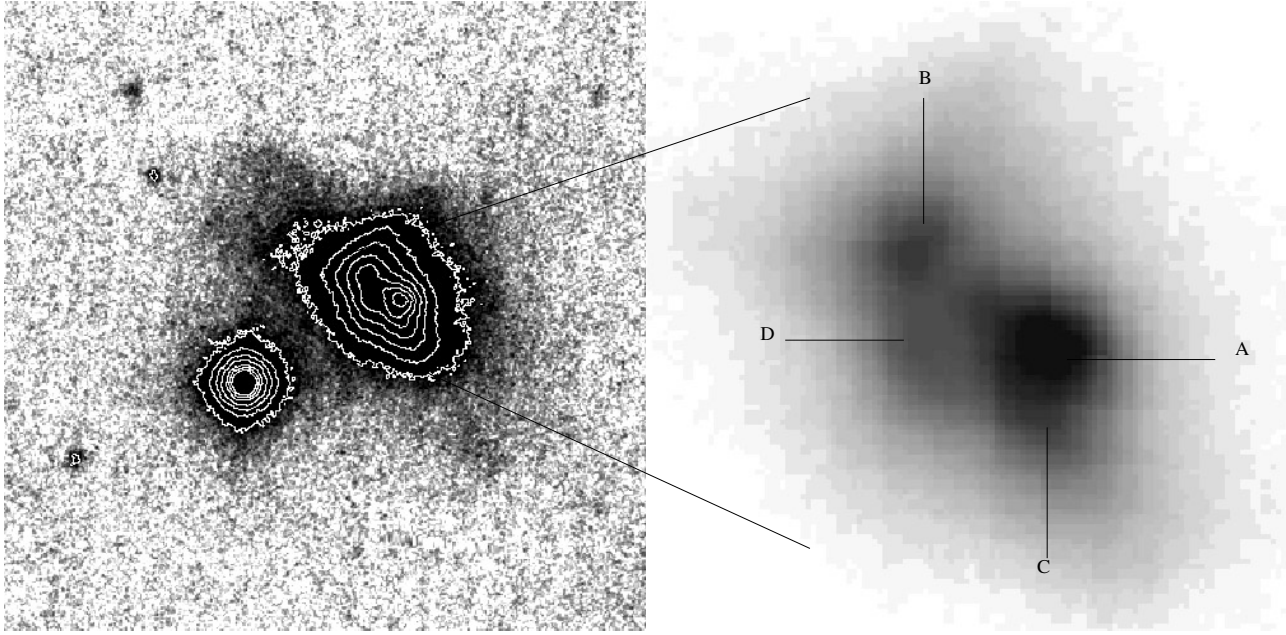
Fig. 1. B+V+R stacked image of Mkn 789 in logarithmic grey scale with overplotted intensity contours. The field size is $1.2' \times 1.2'$ and the orientation is north up and east to the left. The central $18'' \times 18''$ region is also shown and four emission regions are identified and labelled. The contours are selected so as to better illustrate the detailed object structure rather than corresponding to some particular surface brightness levels.

Table 2. Photometry in the field of Mkn 789

Region	V	(B-V)	(V-R)
A	16.25 ± 0.04	0.26 ± 0.06	0.47 ± 0.05
B	17.51 ± 0.05	0.25 ± 0.06	0.44 ± 0.05
C	17.37 ± 0.06	0.37 ± 0.08	0.42 ± 0.07
D	17.87 ± 0.06	0.68 ± 0.08	0.69 ± 0.07
Total	14.68 ± 0.04	0.37 ± 0.06	0.42 ± 0.05
star 1	14.97 ± 0.04	0.55 ± 0.05	0.27 ± 0.04
($9''$S, $16''$E)			
star 2	15.96 ± 0.04	0.67 ± 0.05	0.39 ± 0.04
($33''$S, $34''$W)			

In Table 1 we list the objects and the dates, configurations, exposure times and the most relevant parameters of the observations. The data was obtained under photometric conditions and this was verified by comparison of the calibration data obtained during the run.

For the reduction of the spectroscopic data we used a package especially developed at Meudon Observatory. The reduction and calibration procedures were described in detail in Paper I. The resulting compact "spectroscopic image" contains 397 rows, each of them being a spectrum that corresponds to an individual fibre. It is then possible to extract various parameters (flux, central wavelength, line width) in selected emission/absorption lines or wavelength bands for each individual spectrum and use them to "reconstruct" intensity/velocity/dispersion maps. For each two-dimensional spectroscopic image, a mean "sky" spectrum is constructed, using

the fibres that are not contaminated by line emission from the object. However, this is unavoidably contaminated by continuum emission from the object, as the spectrograph covers a small (central) part of each object and no other spectra of "pure" sky were taken. The sky spectrum so constructed is then subtracted from all the individual spectra.

Subsequent analysis was performed using the tasks of the ONEDSPEC package in IRAF, for each fibre spectrum as well as for the "integrated" spectra (sum of many individual spectra) of the structures of interest (nuclei,"hotspots", HII knots). Percentage errors in the measured fluxes (from Gaussian line fits) were calculated in the following way: we plot the deviation of the measured $\frac{[OIII]5007}{4959}$ and $\frac{[NII]6583}{6548}$ minus the theoretical (~ 3) ratios versus the flux of the (faintest) $[OIII]_{4959}$, $[NII]_{6548}$ lines respectively. Assuming that all the error in the measured line ratio is due to error in the flux of the faintest line, the mean deviation per flux bin divided by 3 (the theoretical ratio) will then represent the mean percentage error in the measured fluxes in this particular flux bin. The errors in the measured velocities, are estimated in an analogous way and they remain always within the ± 50 km sec^{-1} precision of our wavelength calibration.

Standard calibration procedures were used for the reduction of the broad band images. The photometric calibration was based on a standard sequence of NGC 2264 (Christian et al. 1985) and checked on standard stars from Landolt (1983), all observed during the same run. The contamination of the observed magnitudes and colours due to line emission from the object were estimated in the following way: for each nucleus or hotspot, we multiply its spectrum with the filter transmission
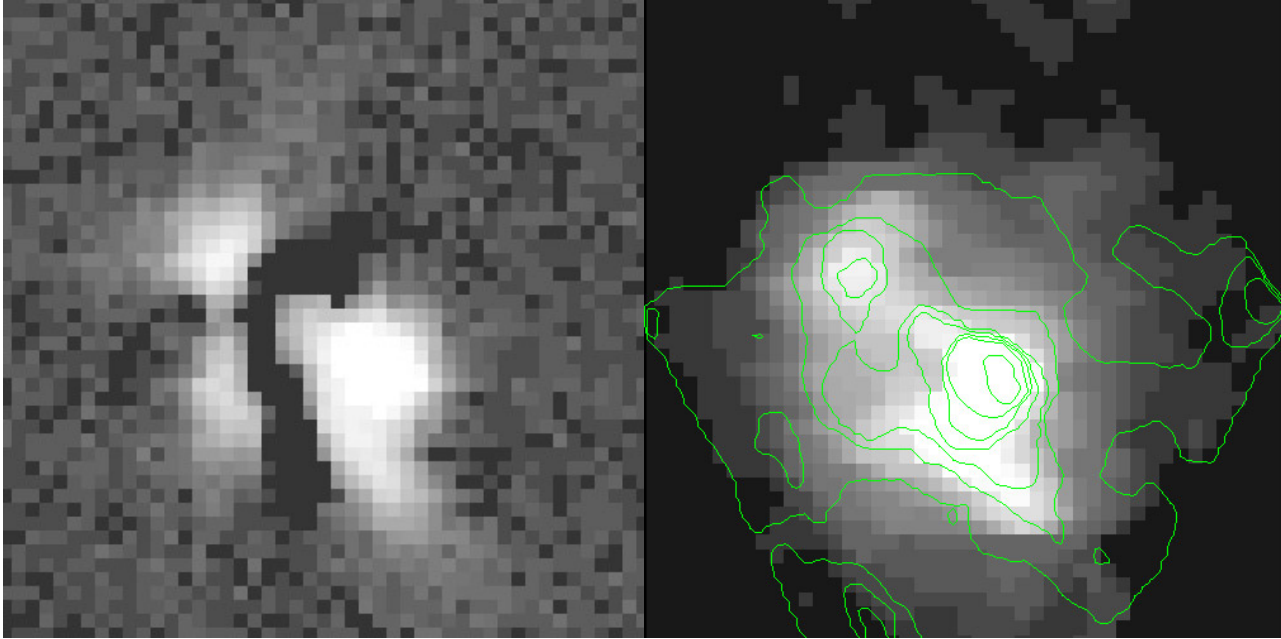
Fig. 2. a Residual R image of Mkn789 in logarithmic greyscales, produced by the technique of unsharp masking (see text). **b** Reconstructed $H\alpha$ intensity image in greyscales and superposed contours of the reconstructed continuum image (both are smoothed with a median filter). The field of view is $\sim 16'' \times 16''$ and the orientation is north up and east to the left.

curves and then integrate the fluxes with and without the emission lines. This allows to estimate the percentage contamination in each band and the corresponding corrections in the measured quantities. This method gives an absolute upper limit of the estimated contamination, due to the fact that we are surely underestimating the object continuum, which is partly subtracted with the sky spectrum, as we discussed above.

For each object we have constructed two-colour maps, after (i) correcting for the geometrical distortion between two broad-band images (because of the chromatic deviation of the spectrograph's optics) and (ii) degrading the image with the best seeing to match the resolution of the other (seeing measures are given in Table 1).

The technique of digital unsharp masking allows enhancement of the sharp features such as nuclei, emission knots or absorption lanes. We have first smoothed the direct images with a large (20 pixel side) median filter and then subtracted the smoothed from the original image, to produce the residual unsharp masked images for each object, that are shown in the corresponding sections.

In what follows we use H_0=75 km sec^{-1} Mpc^{-1} and q_0=0. The redshifts of the three objects corresponding to their systemic velocities are: z=0.0310, 0.0245 and 0.0158 for Mkn 789, UGC 4085 and UGC 3995 respectively (see also Table 9).

3. Mkn 789

Mkn 789 is a well studied galaxy with known multiple nuclei. Veron-Cetty & Veron (1986) and Mazzarella & Boroson (1993) identified two main emission knots that they designated as "nu-

clei", suggesting that this object is an interacting/merging system of two galaxies. Gorjian (1995), using direct images obtained with the WFPC2 of the HST, resolved the main nucleus into three sub-components, aligned along 0.4″. However, because no individual spectral information for the "subknots" is available, it is not clear whether they all are star forming regions or whether any of these knots are actual separate galaxy nuclei. Mkn 789 also shows an extended radio structure (Kukula et al. 1995), offset by $\sim$ 8 arcsec from the optical nucleus, but no compact components (the authors do not give a more precise description). The lack of a conspicuous Seyfert nucleus, the diffuse radio emission and recent spectroscopic data on the two main knots showing HII-like emission line ratios (Mazzarella et al. 1991; Mazzarella & Boroson 1993; Osterbrock & Martel 1993), are all evidence for Mkn 789 being powered by a starburst rather than an AGN.

Our motivation is to establish the nature of the various components of this object and search for kinematical signatures of a recent interaction. We have carried out bidimensional spectroscopy of the central 16 x 16 arcsec region which includes all the putative nuclei. Our resolution of 0.7″/fibre, although not good enough to distinguish these subknots, is sufficient to study the dynamics and starburst activity on the arcsecond scales.

3.1. Direct images and photometry

In Fig. 1 we show the sum of B, V and R images in a $1.2' \times 1.2'$ field and the R image of the inner region ($18'' \times 18''$) where we identify four emission regions labeled A, B, C and D. The structures A and B are identical to, respectively, the nu-
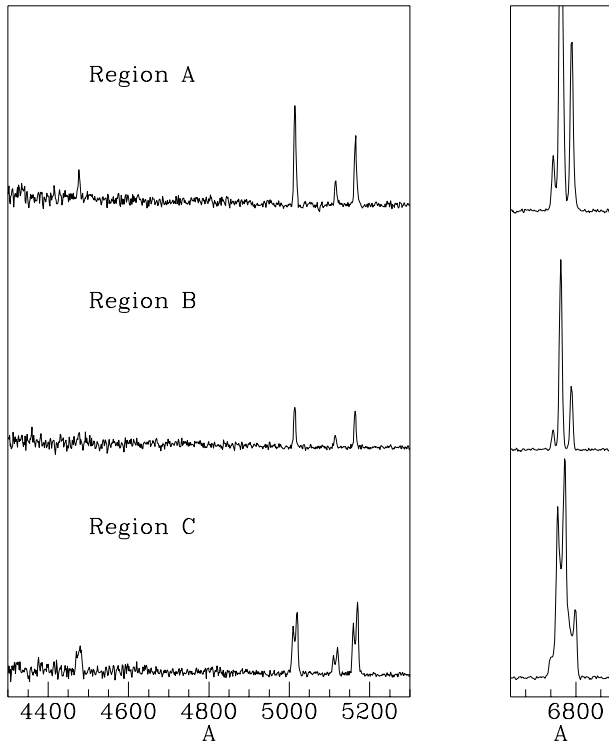
Fig. 3. Averaged spectra for the three main emitting regions of Mkn 789. For clarity we show only selected parts of the observed spectral range (see text). The flux scale is arbitrary but identical for all three spectra.

clei a and b identified by Mazzarella and Boroson (1993). We measure a projected separation of 4.5 arcsec on the B image.

In Fig. 2a we present the R residual unsharp masked image. This is consistent with the HST image published by Gorjian (1995; his Fig. 5) and shows that all four emission regions are extended, although our resolution is not good enough to decompose the structure A in its subknots (the seeing is $\sim 1''$ on the R image).

Table 2 summarizes the photometric measurements for the various components of Mkn 789 and for the two nearest stars in the field (distances in arcsec from knot A are given). The magnitudes have been measured using an aperture of ~ 1.8 arcsec radius centered on each component. We have also measured "total" magnitudes using an aperture of 10.7 arcsec radius (~ 6 kpc).

Contamination due to line emission is estimated as outlined in Sect. 2. In the R band the contamination is a few percent to at most 10% for the regions A and B while it is twice as important for region C, due to its strong $H\alpha$ and $[NII]$ emission lines. Line emission contamination in the other bands is negligible with at most a few percent for C due mainly to the $[OIII]$ (V) and $H\beta$, $H\gamma$ (B) lines. These translate to maximum corrections in the $V-R$ colours of -0.1 to -0.15 mag for C and smaller for A and B. The corrections in the $B-V$ colours are smaller than ± 0.06, i.e., within the uncertainties of the colours for all regions. The photometric measurements given in Table 2 are

the observed values, without applying any of the corrections discussed above.

The three structures A, B and C have similar colours. They are quite blue indicating that these are likely to be star-forming regions. Comparing their colours to starburst models (Bica et al. 1990), if the true colours of regions A, B and C are similar to that of a young stellar cluster ($\sim 10^6$yr), it would imply an extinction (A_V) of 0.5-0.8. This is comparable to the extinction estimated using the observed $H\alpha/H\beta$ line ratios, as we will discuss in Sect. 3.3. A large dust lane is obvious in all direct images and could be the main cause of the distinctive (significantly redder) colour of region D compared to the three others. In this case, assuming that the real colours of D are similar to those of the other regions, it would imply that the extinction in the D direction is one magnitude larger than in the directions of A, B and C. If, on the other hand, the extinction is comparable in all directions, a significant contribution from an older population may be responsible for the redder colours of D.

On a high-contrast R image, a feature resembling a tail emerges NW of the main body and the faintest contour (μ=26.5 mag arcsec^{-2}) can be traced out to 26 kpc. The shape and extension of the structure B is pointing towards the direction of the tail in agreement with the suggestion of Gorjian (1995) that this is probably a bright tidal arm. A luminous extension to the north-east (direction of B), resembling a loop of emission, contributes to the irregular appearance of this object.

3.2. Reconstructed images and spectroscopy

We have reconstructed intensity images at wavelengths corresponding to redshifted H_α, H_β and $[OIII]_{5007}$ lines. All of these emission line images have very similar morphologies. Fig. 2b shows a greyscale H_α intensity image with contours of the continuum light superposed on it. The field of view, in the F/8 configuration that we used for Mkn 789, has a diameter of 16$''$(see Table 1). The structures A and C show relatively strong emission lines while B is also visible, but less prominent than either A or C. In the continuum, A is prominent but we also see some emission from regions B and D. In the integrated spectra, the continuum is bluer for C and becomes redder for A. Line emission from the structure C is very bright in the region $\sim$ 2.5$''$SE of A and becomes progressively fainter as it extends (by $\sim 3''$) to the SW. For the sake of presentation of the results we will refer to the main bright region C as "Ce" and to its fainter SW extension as "Cs".

We have constructed the $\frac{H_\alpha}{H_\beta}$ intensity image from the measured ratio on the individual spectra. This image has a morphology similar to the V-R colour map. This spatial coincidence probably indicates that reddening is the main source of the different colours, which occurs mainly in the regions A and D, increasing from west to east throughout the object.

For Mkn 789 we used a grism that covers the spectral range 4200-6900Å. We detected all the main optical emission lines except for the redshifted $[SII]_{6716,6731}$ lines which fall just outside the spectral range of the observations.
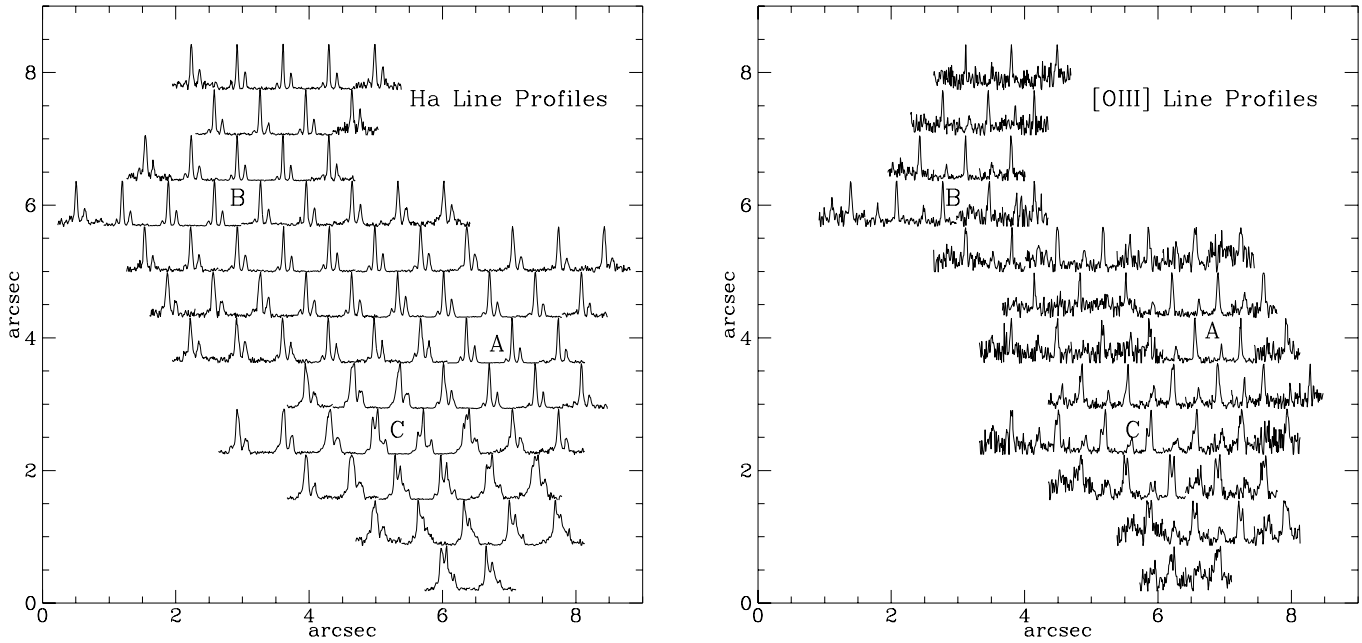
Fig. 4. Spatial distribution of the $H\alpha$, $[NII]$ blend and $[OIII]_{4959,5007}$ line profiles, throughout Mkn 789. The location of the centers of structures A, B and C is indicated with labels. Notice the larger strength and extension of the H_{α}, $[NII]$ lines compared to the $[OIII]$ lines and the multiple line profiles throughout the emitting region C.

Fig. 3 shows three integrated spectra for the regions A, B and C. The spectra are averaged over the three "central" fibres for each region. We only show selected wavelength ranges in order to better illustrate the important emission lines: $H\gamma$, $H\beta$, $[OIII]_{4959,5007}$ in the spectral range 4300-5300 Å and the $[NII]_{6548,6583}$, $H\alpha$ blend in the range 6670-6870 Å.

In Fig. 4 we show the spatial distribution of the H_{α}, $[NII]$ blend and the, overall fainter, $[OIII]_{4959,5007}$ line profiles. Note the profile splitting SE of A, throughout the structure C. We have extracted and processed about 90 spectra in which emission lines were detected.

The H_{α}, $[NII]$ blend was decomposed by fitting the underlying continuum and the lines simultaneously, using the task SPLOT in IRAF. All spectra in the region C have doubly – and sometimes trebly – peaked lines. We used two independent methods in order to decompose the H_{α}, $[NII]$ blend in these complex profiles:

(i) We made use of the IRAF task CONTINUUM in order to fit and subtract the underlying continuum, adjusting the order of the fitted polynomial and the rejection limits in each case. Next, the blend of $[NII]^{6548}_{6583}$ was analysed. The most pronounced $[NII]_{6583}$ (the reddest in most cases) component was fitted, scaled by 1/3, shifted to $\lambda = 6548.1$ Å (based on the ratio of the Einstein A-coefficients under the assumption that collisional de-excitations are not important) and subtracted from the blend. A similar procedure was applied to the residual blend whose blue-most $[NII]_{6548}$ component usually became visible and finally the two H_{α} components were fitted. We considered the fit to be good when the residual intensities were not larger than 3 times the rms intensity of the adjacent continuum. In the

case of triple-peaked line profiles, the decomposition method was similar but it was generally more difficult to reproduce the observed profiles.

(ii) The second method made use of the IRAF task SPECFIT (STSDAS.CONTRIB) package. Here, a model is provided for the continuum and the various initial parameters for gaussian emission line profiles. An interactive fit is then made to the various components via chi-square minimization until the "best fit" values are obtained.

The two methods gave comparable results in most cases and we are confident that the deduced velocities for the individual components are accurate within the error margin. The line fluxes are more likely to be affected by errors in the fitted components; for this reason we used both, the fluxes of the individual components and the "total" fluxes in the analysis below, in order to check the validity of our results. In the few cases where the emission lines were obviously asymmetric but no individual components could be fitted, we used the total line flux. Fig. 5 illustrates two typical cases of spectra with double- and triple-peaked lines, that were fitted following the methods outlined above.

Absorption features were detected in a number of spectra, usually the $NaID_{5893}$ doublet and occasionally the MgI_{5175} blend. Considering that the strength of the $NaID$ lines can be significantly enhanced by interstellar gas contribution (Bica & Alloin 1986) and, since we could not unambiguously identify any other absorption features above the 3σ level (probably diluted by continuum and line emission), we have not corrected the measured Balmer emission line fluxes for underlying absorption. If we are witnessing the early stages of a strong star-
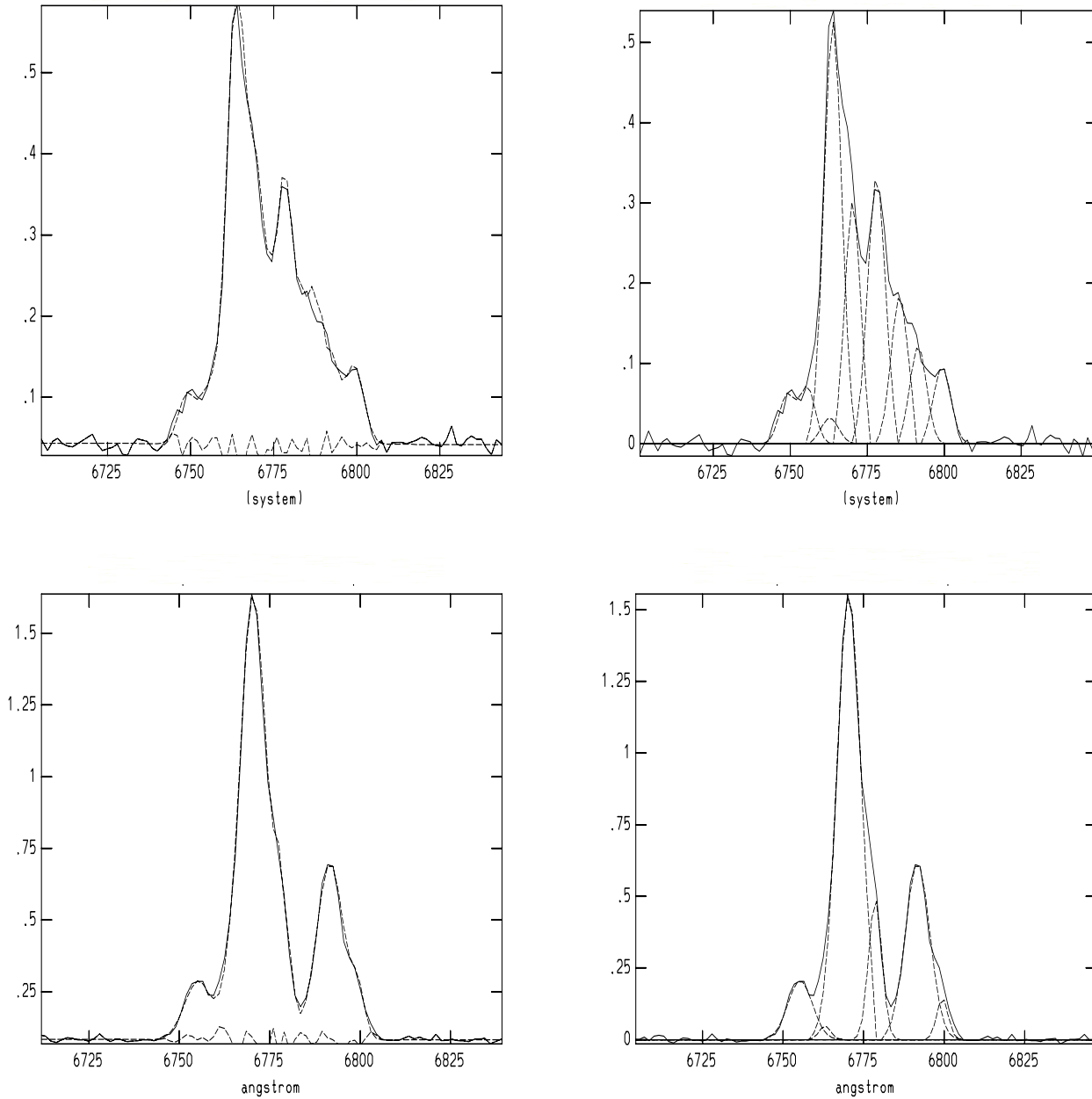
Fig. 5. $H\alpha$, $[NII]$ blend, fitted in the case of double-peaked (bottom panels) and triple-peaked (top panels) lines. Left panels show the observed spectrum (solid line) with the fitted model and the residual (dashed lines) overplotted. Right panels show the observed spectrum (solid line) with the individual fitted components (dashed lines) overplotted (in this second case the underlying continuum has been subtracted).

burst, the emission component from the HII regions probably dominates over the underlying absorption of the old galaxy population. In this case, the Balmer emission would be considerably larger than any Balmer absorption. The uncertainties due to this lack of correction for underlying absorption would affect mainly those spectra with faint H_β emission and would lead to an over-estimation of the $\frac{[OIII]_{5007}}{H_\beta}$ ratio. In some of the line profiles shown in Fig. 4a, one can see red H_α absorption wings, indicating that considerable stellar absorption is present there, the gas being slightly blue-shifted with respect to the stellar velocities. In these cases we are probably underestimating the H_α line flux.

In order to correct the observed line fluxes for internal reddening, we have used the standard relation I(λ)=F(λ) $10^{cf(\lambda)}$ and R=3.1, as in Paper I. The observed line ratio $\frac{F(H_\alpha)}{F(H_\beta)}$ varies considerably throughout the object from values close to the theoretical ratio ~ 3.1 on the west, to ratios as large as 8 on the east, around region D. We have only considered fluxes where both H_α and H_β line intensities are above 3σ of the noise level, while for regions where H_β was too faint we have adopted the $\frac{F(H_\alpha)}{F(H_\beta)}$ ratio of the adjacent regions.
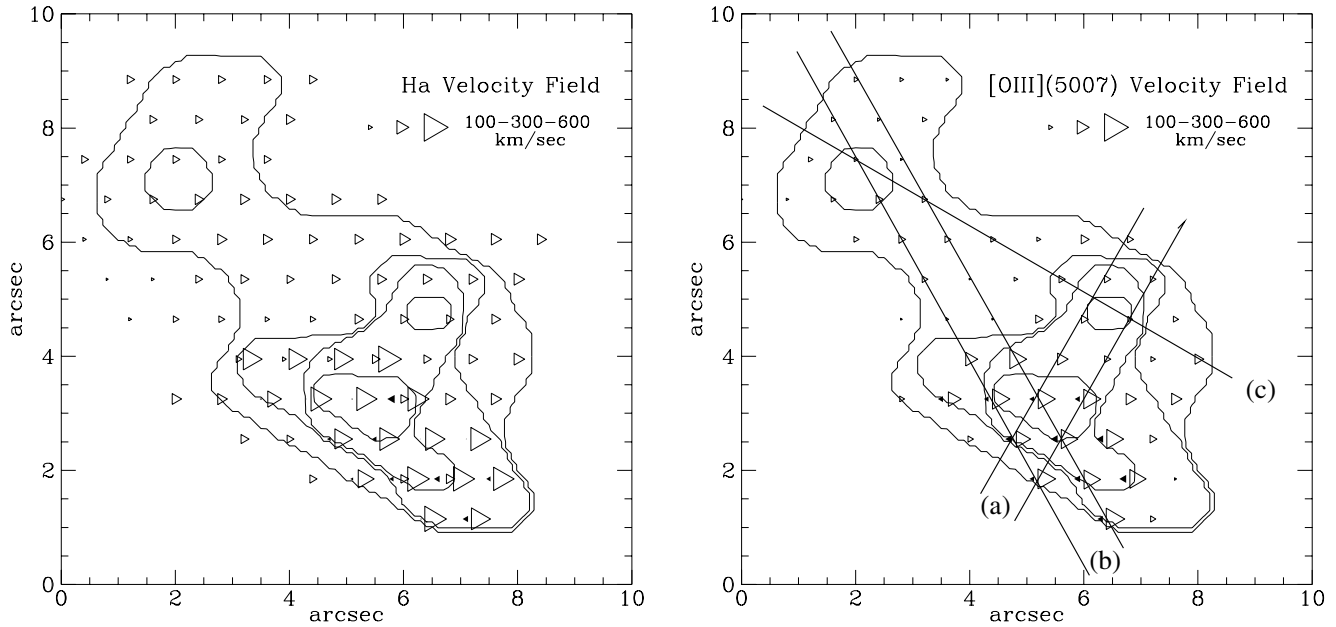
Fig. 6a and b. Spatial distribution of **a** H_α and **b** $[OIII]_{5007}$ velocities for Mkn 789. Filled/open triangles represent blue/red shifts respectively, from the systemic velocity 9305 km sec^{-1}. Notice the region of multiple components (see also text).

The observed line widths were deconvolved with the "instrumental" line width measured from the sky lines, for each individual spectrum.

Finally, in order to calculate a mean "systemic" velocity, we constructed "global" profiles for all the main emission lines, by adding together the individual spectra over the whole object (see also Amram et al. 1995). We calculated midpoint and barycentric velocities that within our uncertainties of ± 50 km s^{-1} are comparable for each line, indicating that the mean line profiles are symmetric. On the other hand, the velocities for the $H_\alpha, [NII]$ blend are larger by ~ 150 km sec^{-1} than for the H_β and $[OIII]_{5007}$ lines. This shift is probably due to a systematic distortion effect at the red edge of the spectrum where the blend was placed, but could not be better accounted for during the wavelength calibration. We adopt a heliocentric "systemic" velocity deduced from the $H_\beta, [OIII]$ lines: 9390$\pm$50 km sec^{-1}, that mainly represents the mean emission line velocity rather than the true systemic velocity. The latter is measured to be 9305$\pm$50 km sec^{-1} from 21cm data (Martin et al. 1991), which within the errors and uncertainties agrees with the emission line velocity. For the discussion that follows, we shall refer to "velocities" as the (relative) velocity shifts from the true systemic velocity, rather than the absolute measured velocities.

3.3. Ionization and kinematics

(a) *Flux ratios*

The first part of Table 3 contains the most important line ratios for the regions A, B, Ce and Cs, where the line fluxes are summed over several fibres. In the last column we list the corresponding projected areas in arcsec^2. The second part of the table contains the flux surface brightnesses (line flux per unit of emitting area) in units of 10^{-15} erg sec^{-1} cm^{-2} arcsec^{-2}. For each line we also provide the percentage $flux$ errors, calculated as described in Sect. 2. The $[OIII]$ surface brightness of region C is two and five times that of regions A and B respectively, while that of the Balmer and lower ionization lines is comparable between regions A and C and, in all cases, smaller by more than an order of magnitude for region B.

All fluxes and flux ratios are corrected for reddening, by applying a "mean" $\frac{H_\alpha}{H_\beta}$ ratio of 5.5 for A and 5 for both B and C. These values imply an extinction (A_V) of ~ 1.5 magnitude overall, but the Balmer decrement on the individual spectra over the regions A and C suggests an extinction of ~ 0.9 which is comparable to that estimated from the observed colours (see Sect. 3.1). Adopting a mean value for the Balmer decrement might result in an underestimate of the fluxes on those individual fibres, where we have measured larger reddening, i.e., east of the region A, towards D (see Sect. 3.2). In the region D, the spectra are mainly dominated by continuum light and only some faint Balmer (H_α) and $[NII]_{6548,6583}$ emission is present. This might suggest a redder population in this region, although larger absorption is certainly present, in agreement with our photometry results (3.1). The $[OI]_{6300}$ line was detected only from A, C and in the "absorption zone" between A and B.

To investigate the ionization state of the gas, we plotted in Figs. 16a-c the usual diagnostic line ratio diagrams (Veilleux & Osterbrock 1987), namely log[$\frac{[OIII]_{5007}}{H_\beta}$] vs (a) log[$\frac{[NII]_{6583}}{H_\alpha}$], (b) log$\frac{[SII]_{6716+6731}}{H_\alpha}$] and (c) log[$\frac{[OI]_{6300}}{H_\alpha}$], from the dereddened line ratios listed in Table 3, together with the results for UGC 4085 and UGC 3995. The various points for Mkn 789 are represented by filled squares in these figures.
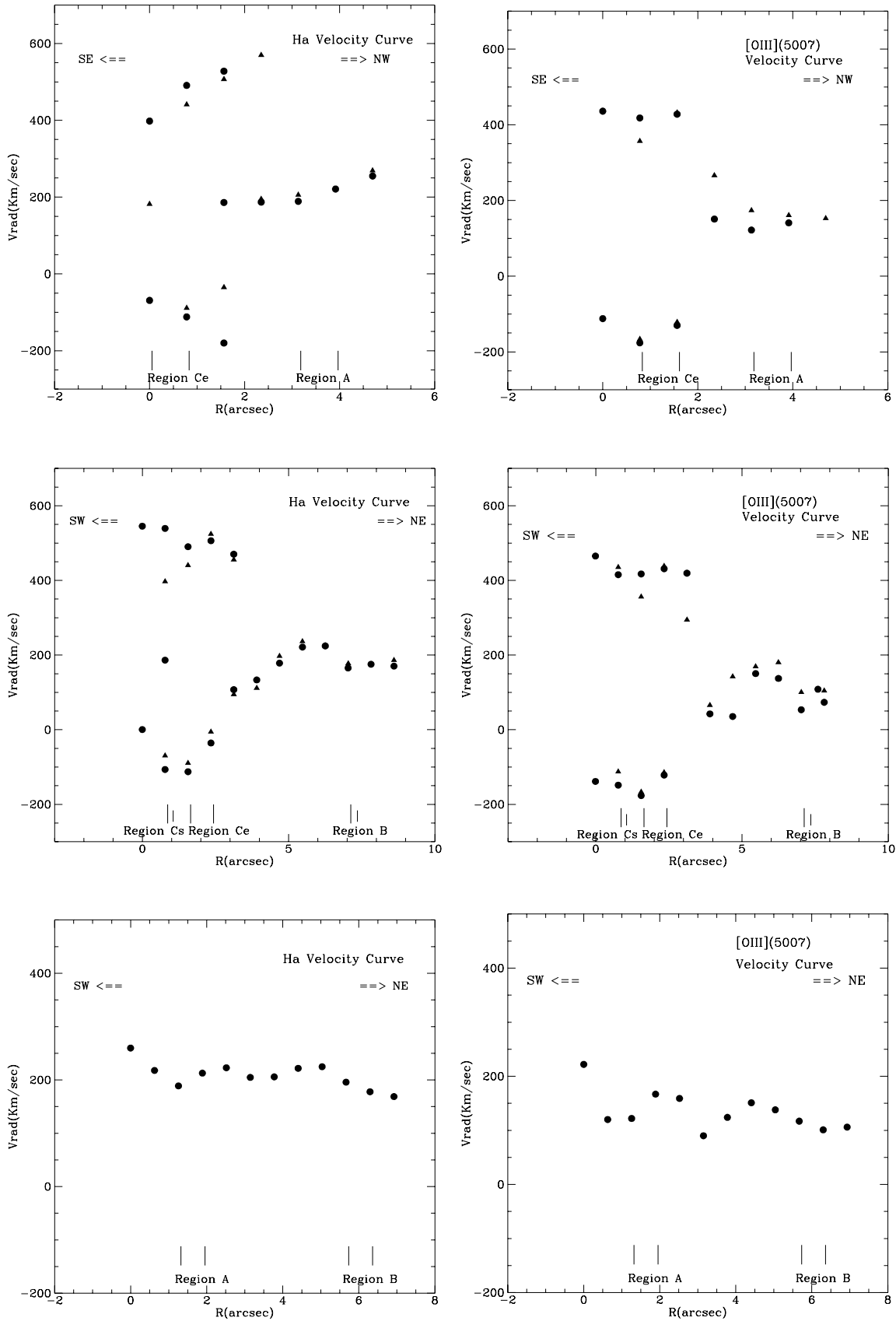
Fig. 7a–c. Radial velocity curves for the $H\alpha$ and $[OIII]_{5007}$ lines along three directions: **a** PA$\sim 158^o$ (upper boxes) **b** PA$\sim 26.5^o$ (middle boxes) **c** PA$\sim 56^o$ (bottom boxes). Velocities are shifts from the adopted V_{sys}=9305 km sec^{-1} and the "central" positions of the various emitting regions are indicated as well. For each direction we plot velocities along a line passing through the region centers (filled circles) and a second one passing 0.7$''$(one fibre) north (**a**) or east (**b**) of the centers.
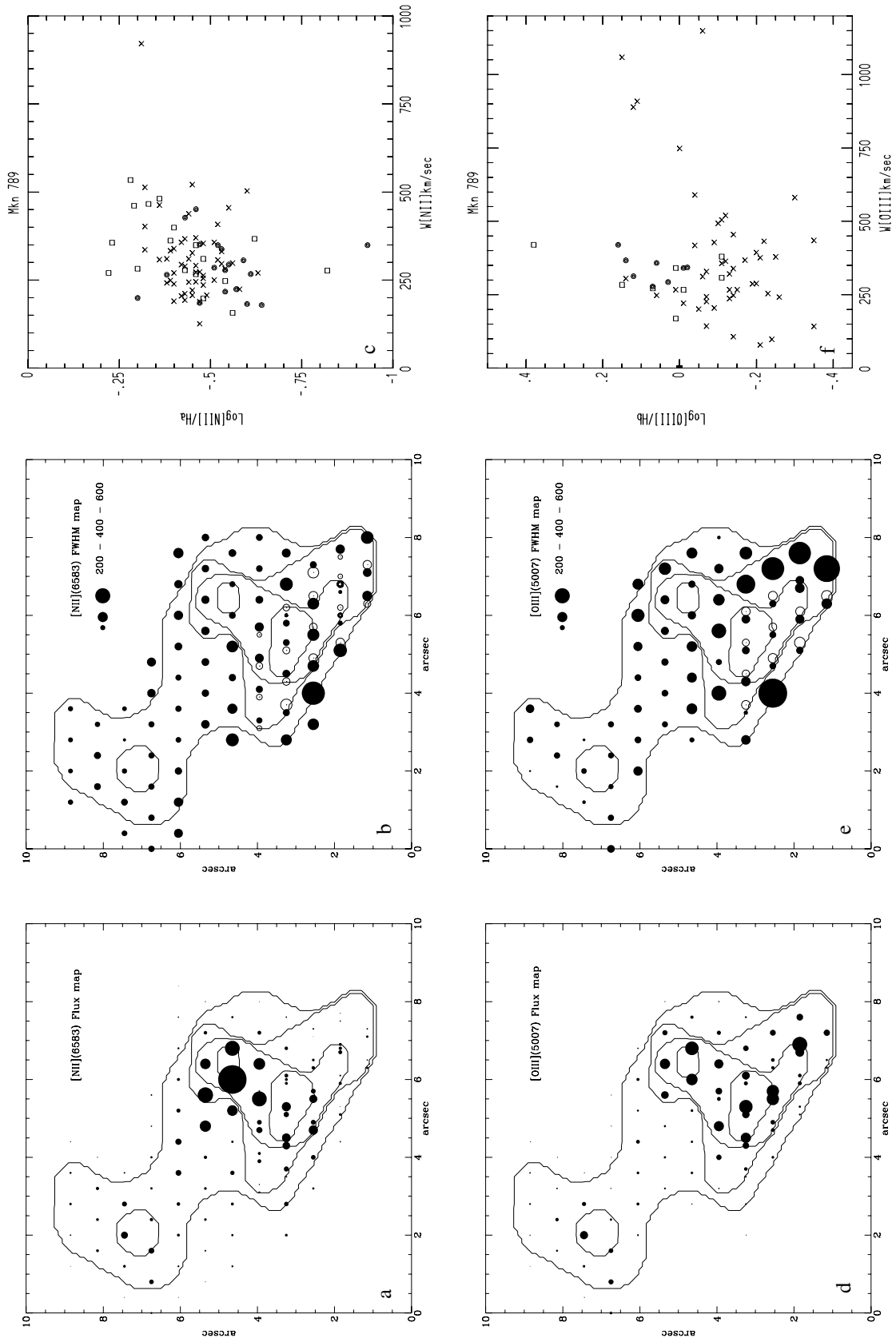
Fig. 8a–f. Spatial distribution of the $[NII]_{6583}$ and $[OIII]_{5007}$ line fluxes **a**, **d** and FWHM **b**, **e** for Mkn 789. Flux values range up to 11.3×10^{-15} ergs cm^{-2} sec^{-1} for $[NII]_{6583}$ and 3.2×10^{-15} ergs cm^{-2} sec^{-1} for $[OIII]_{5007}$. In the plots of FWHM($[NII]_{6583}$) vs log($\frac{[NII]_{6583}}{H_\alpha}$) **c** and FWHM($[OIII]_{5007}$) vs log($\frac{[OIII]_{5007}}{H_\beta}$) **f** simple crosses represent total fluxes whereas crosses inside boxes/circles represent blue/red shifted components respectively.

Table 3. Line ratios and flux densities for the gas in Mkn 789

Region	$\text{Log}\frac{[OIII]_{5007}}{H_\beta}$	$\text{Log}\frac{[NII]_{6583}}{H_\alpha}$	$\text{Log}\frac{[OI]_{6300}}{H_\alpha}$	$\frac{H_\alpha}{H_\beta}$	$\frac{H_\gamma}{H_\beta}$	Area
A	-0.14	-0.43	-1.56	5.5±0.9	0.2±0.05	3.08
B	-0.07	-0.48	-	5.3±0.8	-	1.54
Ce	0.002	-0.47	-1.72	5±0.6	0.34±0.05	1.92
Cs	0.12	-0.49	-1.50	5.2±0.7	0.23±0.04	1.15

Region	SH_β	$S[OIII]_{5007}$	$S[HeI]_{5875.6}$	$S[OI]_{6300}$	SH_α	$S[NII]_{6583}$
A	36.77 15%	26.45 15%	4.29 19%	3.79 21%	137.48 6%	50.48 8%
B	14.72 13%	12.64 13%	1.45 25%	-	46.90 7%	15.48 10%
Ce	37.97 11%	38.19 10%	2.93 20%	2.14 20%	111.58 6%	37.91 8%
Cs	17.25 12%	22.90 11%	2.55 21%	1.92 18%	23.71 7%	19.65 9%

All fluxes and line ratios are corrected for internal reddening except for the $\frac{H_\alpha}{H_\beta}$ and $\frac{H_\gamma}{H_\beta}$ ratios. The flux densities are expressed in units of 10^{-15} erg sec^{-1} cm^{-2} arcsec^{-2}. The projected emitting areas are expressed in arcsec^2 and correspond to 1.03 kpc^2 for A, 0.52 kpc^2 for B, 0.64 kpc^2 for Ce and 0.39 kpc^2 for Cs. Next to the flux densities we list the percentage error in the line fluxes (see text).

Table 4. Photometry in the field of UGC 4085

Object	V	(B-V)	(V-R)
Knot A	17.37 ± 0.04	0.73 ± 0.06	0.61 ± 0.05
Knot B	17.88 ± 0.04	1.05 ± 0.06	0.71 ± 0.05
Knot 1	18.67 ± 0.04	0.52 ± 0.06	0.57 ± 0.05
Knot 2	18.78 ± 0.04	0.52 ± 0.06	0.66 ± 0.06
Knot 3	18.98 ± 0.05	0.56 ± 0.07	0.65 ± 0.07
Total	14.01 ± 0.03	0.70 ± 0.05	0.46 ± 0.04
star 1 (13″N, 45″W)	15.85 ± 0.03	1.35 ± 0.05	0.85 ± 0.04
star 2 (14″S, 34″W)	16.76 ± 0.03	0.98 ± 0.05	0.45 ± 0.04

All regions of Mkn 789 fall well within the loci of HII regions, indicating that these are photoionized by hot stars. However, we do note a progression towards higher $[OIII]_{5007}$ and $[OI]_{6300}$ relative strengths (i.e., towards higher ionization) from structures A through B towards Ce and Cs. For A and B our values for the $\frac{[NII]_{6583}}{H_\alpha}$ and $\frac{[OIII]_{5007}}{H_\beta}$ ratio are consistent with those given by Mazzarella & Boroson (1993; they only measured upper limits for the $\frac{[OI]_{6300}}{H_\alpha}$ ratio). The error bars are derived from the % errors in the line fluxes, estimated as described in Sect. 2 and they account mainly for the uncertainties associated with the flux calibration, the photon noise and uncertainty in the decomposition of the H_α,[NII] blend, especially in the case of multiple components affecting regions Ce and Cs. These errors do not account for any:

(i) underestimation of the H_β flux in those few spectra where stellar absorption lines are present (this does not affect significantly the "summed" line ratios in Fig. 16),

(ii) uncertainty in the internal reddening correction. This does not appear to be an important source of error, because the distribution of points on the diagnostic diagrams that we constructed using the uncorrected flux ratios, is comparable with that for the corrected ones.

In Fig. 16d we plot $\frac{[OIII]_{5007}}{H_\beta}$ vs $\frac{[NII]_{6583}}{H_\alpha}$ for the individual components of multiple profile lines, for comparison with the "summed" line ratios. Here, open/filled symbols represent the blue/red shifted components respectively. On regions Ce (diamonds) and (SE of) A (square), the redshifted component dominates all line profiles (as can also be seen in Fig. 4) and shows higher ionization line ratios than the blueshifted component. Towards Cs the situation becomes reversed: the blueshifted emission is strengthened and the approaching gas shows higher $[OIII]_{5007}$ and $[OI]_{6300}$ relative ratios. One should interpret these results with caution, as the line fluxes of individual components are critically dependent on how accurately the line profiles were deblended.

(b) *Velocities*

Figs. 6 (a) and (b) show the spatial distribution of velocities for the H_α and $[OIII]_{5007}$ lines. Filled/open triangles represent blue/red-shifts respectively. We note again the overall larger velocities deduced from the H_α line, as discussed above. Velocity fields that we constructed for other emission lines are comparable.

Fig. 7 shows the radial velocities for $[OIII]_{5007}$ and $H\alpha$ along three directions: (a) PA$\sim$ 158° between regions Ce and A, (b) PA$\sim$ 26.5^o on the line connecting regions Cs, Ce and B and (c) PA$\sim$ 56° between regions A and B, which are also indicated on Fig. 6(b). In each direction we plot the velocities along two adjacent lines, one that transverses the centers (maximum intensity) of the indicated regions, denoted by circles, and one that passes 0.7″(one fibre) N (8a) and E (8b) of the centers, denoted by triangles. As there is no clear nucleus we assume the zero point in the distance axis to be at the starting (southern) point of each direction.

In both Figs. 6 and 7, the velocities are represented as shifts with respect to the systemic velocity V$_{sys}$=9305 km sec^{-1} (Martin et al. 1991). In the region C, violent gas motions occur as evidenced by the profile splitting, while outside this region the gas appears to be kinematically quiescent. The line splitting starts 2 arcsec SE and 2.5 arcsec SW of the centers of regions A and B respectively. It is larger in the SE-NW direction (upper boxes), where the velocity separation reaches 550-600 km sec^{-1} for $[OIII]$ and 700 km sec^{-1} for $H\alpha$. In both directions, the

velocity separation is symmetric about the mean velocity of the gas outside the split region (which is ~ 50 km sec^{-1} for $[OIII]$ and ~ 150 km sec^{-1} for $H\alpha$). The velocity split of the two components is also symmetric about the "middle" component, whenever triple profiles could be reasonably deblended.

Throughout the regions A and B the velocity remains ~ 100-200 ± 50 km sec^{-1} and along the direction that connects them (bottom boxes) there is no appreciable structure in the velocity field, except for a smooth general decrease in velocity from SW to NE. The two smaller amplitude patterns of δV=+50 km sec^{-1} seen especially in the $[OIII]$ line profiles, are probably real and correspond to the knots of emission popping up from the heavy extinction, between A and B (see Fig. 1). In the direction of region D, from the little emission that is detected, the velocity is within 100 km sec^{-1} from the systemic.

In Fig. 8 we show the spatial distribution of the $[OIII]_{5007}$ and $[NII]_{6583}$ line fluxes and FWHM, in an attempt to compare the two data sets. Also plotted in this figure are the FWHM($[OIII]_{5007}$) vs log($\frac{[OIII]_{5007}}{H_\beta}$) and FWHM($[NII]_{6583}$) vs log($\frac{[NII]_{6583}}{H_\alpha}$). The distribution of line widths is tightly correlated with the velocity field as it would be expected if the mechanism that drives material radially is also responsible for broadening the line profiles. The narrowest profiles occur in region B, with less than 250 km sec^{-1} for $[OIII]$ and $[NII]$ and ~ 250-300 km sec^{-1} for the Balmer lines, which are typical for HII regions. All lines become broader, with FWHM$\sim$ 300-350 km sec^{-1}, in the optical absorption region and in region A. The broadest profiles occur in the boundaries of the line splitting region, with FWHM$\sim$ 400-900 km sec^{-1}, where both individual velocity components may be present but not resolved with these data. This results in the asymmetric and very large profiles that we observe in this region. Throughout the region C each of the two (resolved) components has a FWHM of $\sim$ 250-450 km sec^{-1}. There is a rather good correlation between $[NII]$ line widths and the $\frac{[NII]_{6583}}{H_\alpha}$ line ratio, considering that the errors associated with deblending of the split profiles must contribute significantly to (and probably dominate) the scatter in this plot. On the other hand, the correlation between the $[OIII]$ line widths and the $\frac{[OIII]_{5007}}{H_\beta}$ line ratio is weak. Here, the large scatter towards smaller line widths is certainly real, the components of the split profiles showing the largest ionization. The largest ($\gtrsim 500$ km sec^{-1}) line widths correspond to unresolved double profiles and the correlation in Fig. 8f would not exist at all if we could resolve the individual components, as all points would move on the left of 500 km sec^{-1}.

We will discuss further these results in Sect. 6.

4. UGC 4085

4.1. Direct images and photometry

Until now relatively few studies have been carried out for this object. On a direct R band image shown in Fig. 9a, it appears as an asymmetric spiral galaxy with two central condensations, one of which is embedded in a bar-like structure. In Fig. 9b we show the central $(44.5$ arcsec$)^2$ region of the residual R band
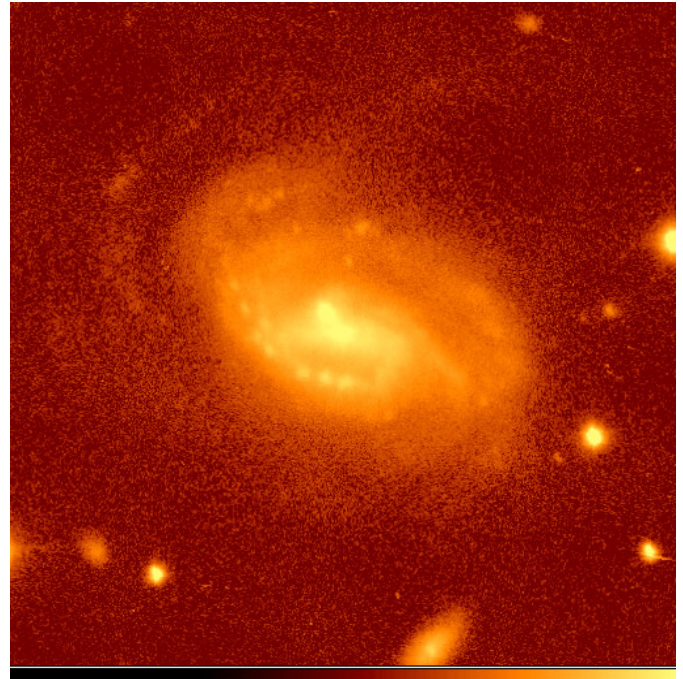

Fig. 9a. R band image of UGC 4085 in logarithmic grey scale; field size is $2.2' \times 2.2'$ and orientation is north up and east to the left.

image produced by digital unsharp masking (as described in 2) where we have identified and labelled the two central regions A, B and the three brightest southern emission knots 1-3. This figure clearly shows the spiral structure dominated by giant HII regions. A bar-like structure extends along $\sim$ 18 arcsec ($\sim$ 8 kpc) in the E-W direction and spiral arms start from its edges, that wind tightly around the main body and are splitting in two at $\theta \sim 180^o$.

The photometric measurements for the various components and the two brightest stars in the field are summarized in Table 4. These are the observed values, uncorrected for any emission line contamination. We measured magnitudes using an aperture with radius 1.2 arcsec for B and V and 1.4 arcsec for R for the knots and the stars. We also give magnitudes for the whole galaxy, measured in an aperture of 120 pixels radius (~ 9.8 kpc) that corresponds to a surface area of $\sim$ 0.4 arcmin^2.

The effect of contamination in the magnitudes and colours due to line emission from the object is more important in the R band (due to the $H\alpha$, $[NII]$ lines) with a maximum of 15% for knots 1 and 2 and only a few percent for the other knots. Contamination in the other two bands remains comparable to the uncertainties of the measurements. Consequently, the corresponding colour corrections are within the error limits in $B-V$ for all knots, while in $V-R$ they could reach 0.15 mag for knots 1 and 2.

The galaxy as a whole is blue with significant reddening in the central region and large absorption bands on the far side (Fig. 9a). The much redder colour of knot B compared to knot A, is obvious on the $B-V$ colour map of Fig. 9c. The three bright HII regions have very similar and relatively blue colours. If we
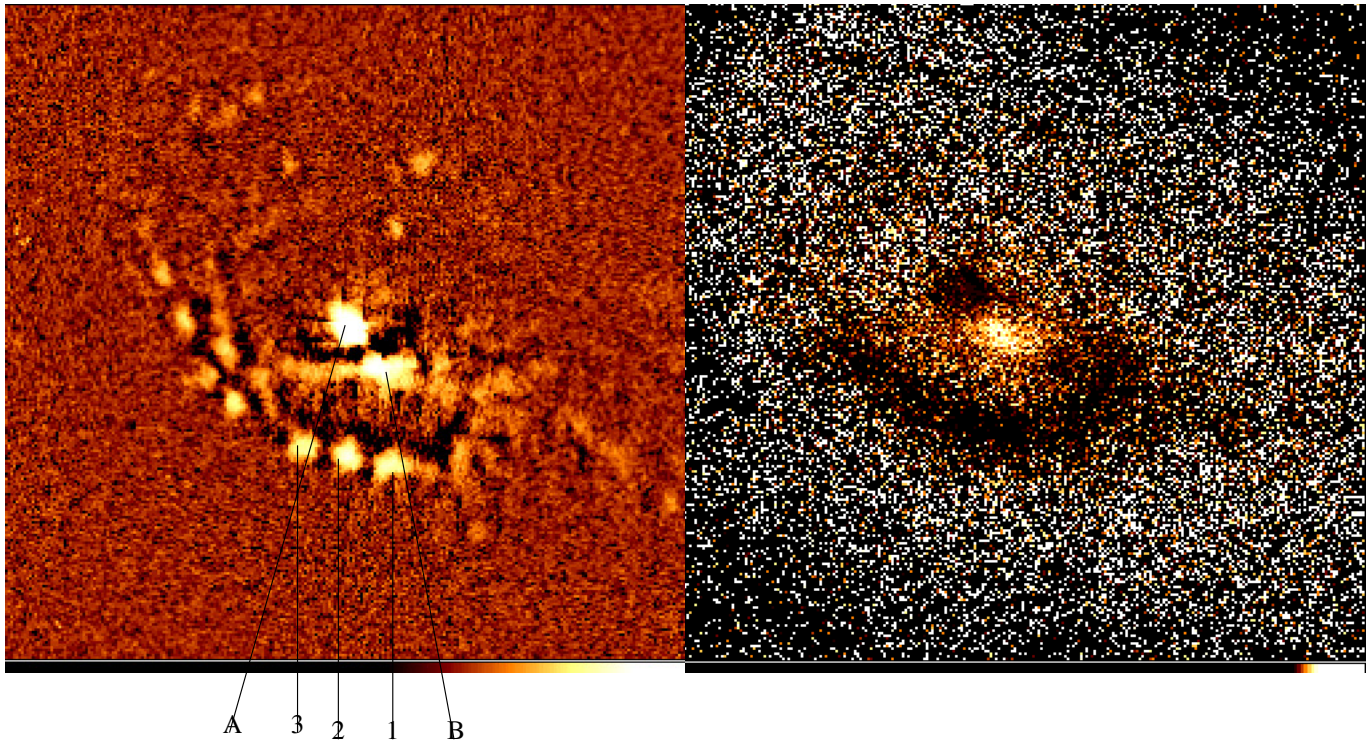
A   3   2   1   B

Fig. 9. b Residual R image produced by digital unsharp masking and **c** $B–V$ colour map (darker are bluer regions). On both images the field size is $44.5'' \times 44.5''(20.4 \times 20.4$ kpc) and the orientation is north up and east to the left. On the residual image the main knots of emission are identified and labelled.

compare the colours of knots 1-3 to those of a young starburst, as computed by Bica et al. (1990), we derive an optical extinction A_V of ~ 1.4 mag. If knot A is a giant circumnuclear HII region as well, its colours imply an extinction of ~ 2 mag. The red colours of knot B might be partially due to an older stellar population, as would be the case if knot B was the, heavily obscured, bulge of the galaxy.

4.2. Reconstructed images and spectroscopy

We reconstructed intensity images for UGC 4085, in the blue and red continuum as well as intensity and velocity maps for the Balmer lines. The field of view has a diameter of $16''$. In Fig. 10b we show the blue continuum image (5300-5500 Å) and in 10c,d the intensity and velocity field respectively of the ionized gas, through the $H\alpha$ line emission.

The knot A and the southern spiral arm are strong H_α emitters, while the strongest sources of continuum light are the knots A and B. This is an indication that knot B might indeed be the location of the galactic nucleus.

Absorption features were detected in only a few spectra. Consequently, as in the case of Mkn 789, we decided not to correct the Balmer line fluxes for underlying absorption. This might result in overestimation of the real $\frac{F(H\alpha)}{F(H\beta)}$ line ratio in these regions. Indeed the observed ratio is quite large, of the order of ~ 4.5 on knots 1-3 but as high as 7.5 in the central regions. While larger reddening in the central regions is certainly

plausible as indicated by our photometry, we have chosen to conservatively adopt the same value for the Balmer decrement, $\frac{F(H\alpha)}{F(H\beta)}$=4.5, throughout the object. This value implies an optical extinction A_V of 1.4 mag which agrees with the extinction estimated from the observed colours (Sect. 4.1). We then proceed to the correction of the observed line fluxes for internal reddening, as described in 3.2

In order to calculate a "systemic" velocity for UGC 4085, we have constructed "global" profiles for the $H\alpha$, $H\beta$ and $[NII]$ lines and calculated the midpoint and barycentric velocities as in the case of Mkn 789. We deduce an heliocentric "systemic" velocity of ~ 7350 km sec^{-1} ± 50km sec^{-1} which is in good agreement with the value of 7328 km sec^{-1} given by Michel et al. (1988). Since there are no measures of the true systemic velocity published for this object, in what follows we will refer to velocity shifts relative to our "systemic" value of 7350 km sec^{-1}.

4.3. Ionization and kinematics

(a) *Flux ratios*

To investigate the ionization conditions and kinematics for this galaxy, we derived fluxes and velocities for individual points corresponding to each fibre spectrum and also for the five "integrated" spectra of knots A, B, 1, 2 and 3 produced by summing up the spectra in the region of each component. The averaged spectra (over three fibres each) for knots A, B, 1 and 2 are shown
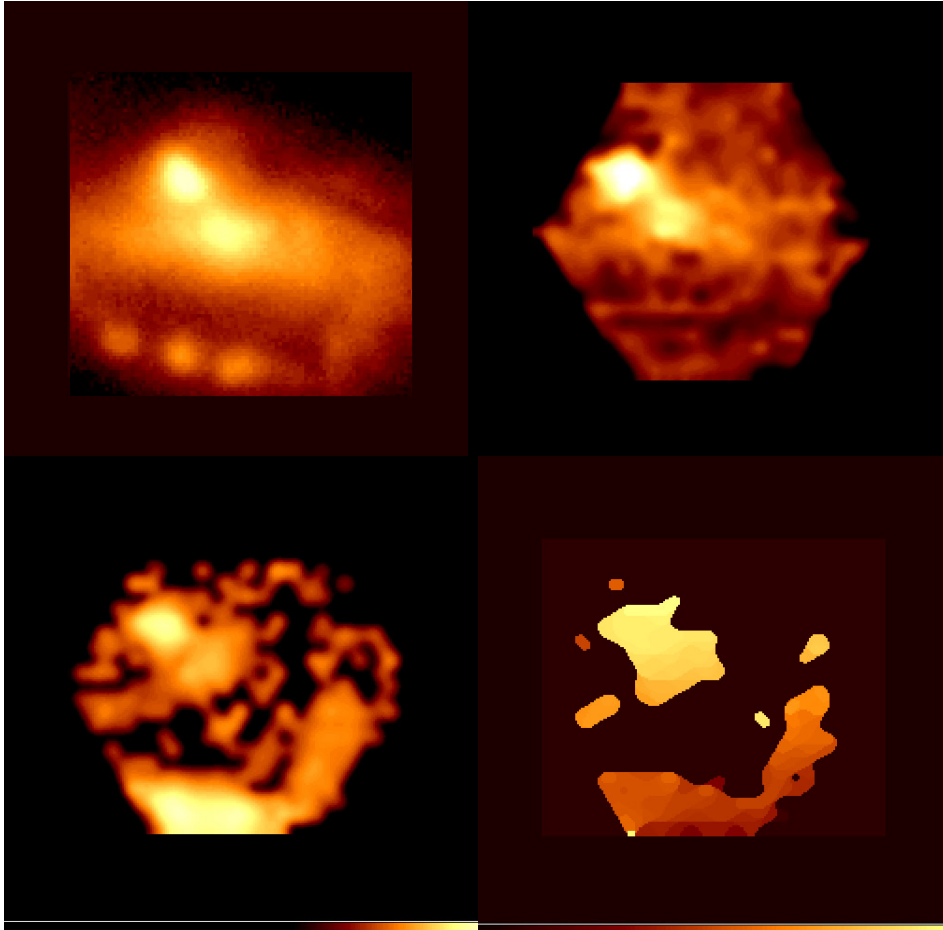
Fig. 10. a The $16.1'' \times 16.1''(7.4 \times 7.4$ kpc) central region of UGC 4085 on the R band, to be compared with the reconstructed images in the same region: **b** 5300-5500 Å continuum light and **c** $H\alpha$ line emission distribution. **d** Velocity map of the $H\alpha$ line, dark to light scale corresponds to velocities of 7200 to 7500 km sec^{-1}. All images are in logarithmic intensity scale. The reconstructed images are smoothed with a median filter

in Fig. 11. As for Mkn 789, we show two selected wavelength ranges containing the most important emission lines: The $H\beta$ line in the range 4900-5200 Å and the $[NII]_{6548,6583}, H\alpha$ blend and $[SII]_{6716,6731}$ lines in the range 6640-6940 Å.

In Fig. 12 we show the spatial distributions of the $H\alpha$ line profiles and of the Log$\frac{[NII]_{6583}}{H\alpha}$ line ratio.

Table 5 contains the various line ratios measured from the integrated spectra. We also list the flux surface brightnesses and the corresponding projected area over which the spectra have been summed for each knot. Finally, we provide the percentage $flux$ errors, calculated as described in Sect. 2.

Very little $[OIII]$ emission is observed, in a few spectra on knot A (and averaged out in Fig. 11). The $H\beta$ line is also generally faint and is most prominent on knots 1 and 2 as are most of the other emission lines. The integrated line ratios for knot A, listed in Table 5, are plotted on the diagnostic diagrams of Fig. 16a-c as filled dots. The error bars are derived from the % flux errors, which appear rather small because the integrated spectra are summed over a higher number of fibres than for the other two objects. Uncertainties related to not correcting for any underlying Balmer absorption and to the adopted reddening correction, are expected to be minimal for the integrated spectrum. All line ratios are characteristic of gas ionized by hot stars, with somewhat higher ionization in the region of knot A. The lower ionization of knot B indicates either a softer ionization spectrum

or that knot B is another giant HII region rather than the true nucleus.

Because the $[SII]_{6716,6731}$ lines are located at the edge of the spectrum and overlap with the OH sky lines, the properties derived from these lines are subject to large uncertainties and are thus only indicative. The measured $[SII]\frac{6716}{6731}$ ratios (listed in Table 5) seem reasonable only for knots A and 1, but too large for knot 2. These ratios imply an electron density N_e of$\sim$ 370 cm^{-3} and ~ 260 cm^{-3} in the region of knots A and 1 respectively (assuming an electron temperature $T_e = 10^4\ ^o$K) which are in the range of electron densities typical for HII regions.

(b) $Velocities$

In Fig. 10d, a reconstructed image of the $H\alpha$ velocity field is shown as grey scale, while in Fig. 13a the spatial distribution of the $[NII]_{6583}$ velocities are represented with symbols whose sizes correspond to shifts from the systemic velocity. The velocities were taken from the overall Gaussian fits rather than from the 80% intensity level (as in Paper I) because the line profiles are rather symmetric (see Fig. 12a) and the velocities deduced using both methods are similar. Indeed, the index of the $H\alpha$ line profile asymmetry at the 20% level (AI_{20}, as in Paper I) was measured to be always less than 0.05.

The general velocity field is smooth throughout UGC 4085, the maximum velocity amplitude being 300±50 km sec^{-1} over a distance of $\sim 13''(\sim 5.8$ kpc). The kinematic axis lies along

Table 5. Line ratios and flux densities for the gas in UGC 4085

Region	Log $\frac{[OIII]_{5007}}{H_\beta}$	Log $\frac{[NII]_{6583}}{H_\alpha}$	Log $\frac{[SII]_{6716+6731}}{H_\alpha}$	Log $\frac{[OI]_{6300}}{H_\alpha}$	$[SII]\frac{6716}{6731}$	$\frac{H_\alpha}{H_\beta}$
A	-0.31	-0.40	-0.70	-1.38	1.24	7.5±0.2
B		-0.29	-	-1.41	-	$\gtrsim$ 7.5
1	-	-0.53	-0.73	-	1.94	4.6±0.1
2	-	-0.49	-0.71	-1.64	2.39	4±0.06
3	-	-0.41	-	-	-	-

Region	SH_β	$S[HeI]_{5875.6}$	$S[OI]_{6300}$	SH_α	$S[NII]_{6583}$	Area
A	1.26 2%	0.14 6%	0.28 4%	6.73 $\lesssim$ 1%	2.68 1%	2.94
B	0.19 4%	0.20 4%	0.09 7%	2.39 1%	1.22 2%	3.43
1	2.98 2%	$\lesssim$ 0.42 5%	-	9.47 $\lesssim$ 1%	2.79 2%	1.47
2	3.27 1%	0.38 3%	0.21 5%	9.08 $\lesssim$ 1%	2.96 1%	2.94
3	-	0.19 6%	-	0.80 3%	2.04 2%	1.96

All fluxes and line ratios are corrected for internal reddening except for the $\frac{H_\alpha}{H_\beta}$ ratio. The flux densities are expressed in 10^{-15} erg sec^{-1} cm^{-2} arcsec^{-2}. The projected emitting areas are expressed in arcsec^2 and correspond to 0.62, 0.72, 0.31, 0.62 and 0.41 kpc^2 for knots A, B, 1, 2 and 3 respectively.
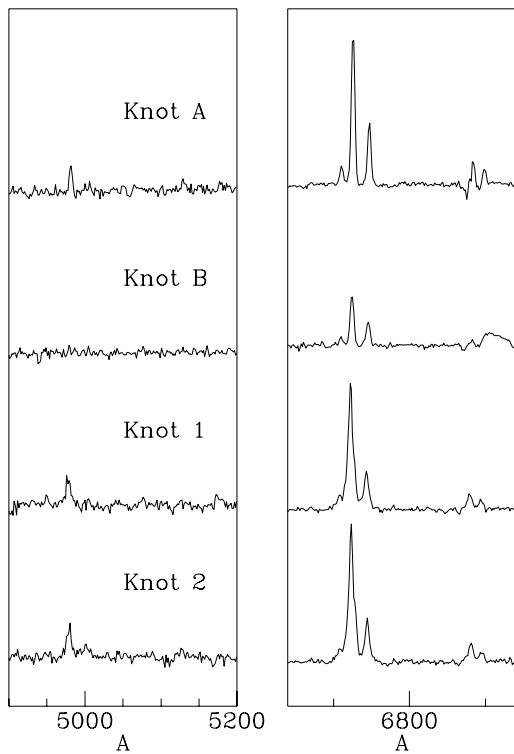

Fig. 11. Averaged spectra for the two central knots A and B and the bright HII regions 1 and 2 of UGC 4085. For clarity we show only selected parts of the observed spectral range (see text). The flux scale is arbitrary but identical for all four spectra.

a SW-NE direction, the southern arm is blueshifted, while knot A is receding with respect to knot B. The western part of the arm, connecting to the central region, appears to have the most negative velocities (-120 to -150 km sec^{-1}). Assuming trailing spiral arms, the projected velocity field implies that NW is the near side and the disk rotates in a retrograde sense.

Fig. 13b shows the distribution of the $H\alpha$ line widths (FWHM), deconvolved with the sky line widths measured on each spectrum. To compare these data sets, we also show the spatial distribution of the $[NII]_{6583}$ and $H\alpha$ line fluxes in Figs. 13 c and d respectively. The $H\alpha$ line widths are smaller than $\sim$ 200 km sec^{-1} in the central regions, but increase up to $\sim$ 350 km sec^{-1} in the star forming knots 1-3. The $[NII]$ line widths are similar but more evenly distributed. The overall small line widths are consistent with the rather low ionization found for this object.

5. UGC 3995

This object is denoted in the CPG catalog (Catalogue of isolated pairs of galaxies in the northern hemisphere, Karatchentsev 1972) as a pair of interacting spiral galaxies, "exhibiting filamentary structure in the form of connecting bridges and tails". It is described as a possible candidate showing a jet emerging from its nucleus (Keel 1985) or, alternatively, being the extension of the arm of the fainter galaxy. The main galaxy has a Seyfert spectrum (Keel 1985, De Grijp et al. 1992) while the companion shows a composite nuclear spectrum with weak $H\alpha$ emission and projected velocity difference of 400 km sec^{-1} (Keel 1985).

UGC 3995 has abnormally red $J - K$ and $H - K$ colours (Cutri & Mac Alary, 1985) and warm mid-IR colours (De Grijp et al., 1987). With a spatial resolution of 1.4 arcsec/fibre (poorer than for the previous two objects), this configuration allowed us to map a larger field (32 arcsec), including some of the spiral structure of the companion.

5.1. Direct images and photometry

Fig. 14a shows the B image 2.1$'$×2.1$'$field, in negative greyscales. In Fig. 14b we show contours of the residual R image produced by the technique of unsharp masking, superposed on the original R image (in negative greyscales). All images are somewhat affected by a saturated star, south of the system. The two galaxies are clearly interacting, a connecting "bridge" being visible in all images and their projected separation is $\sim$ 29.3$''$($\sim$ 8.78 kpc).

Table 6. Photometry in the field of UGC 3995

Object	V	(B-V)	(V-R)
UGC 3395 (bulge)	15.33 ± 0.04	0.90 ± 0.06	0.52 ± 0.06
Companion (bulge)	18.10 ± 0.05	0.70 ± 0.06	0.68 ± 0.06
"J"	20.3 ± 0.3	1.7 ± 0.15	1.05 ± 0.10
star 1 (145″N, 65″E)	15.60 ± 0.04	0.46 ± 0.04	0.22 ± 0.04
star 2 (126″S, 92″W)	15.68 ± 0.04	0.64 ± 0.04	0.46 ± 0.04

Both galaxies are spirals, UGC 3995 is seen at a large inclination while its companion is almost face-on. UGC 3995 has a bright nucleus and shows a rather weak bar-like structure that traces the galaxy major axis. The SE rim of this extended structure is brighter, while on the opposite side it appears fragmented, probably due to dust in the spiral arm of the companion. Two main knotty arms start at $\theta \sim 90^o$ and 180° from the major axis, winding tightly by more than 360° around the main body. Assuming that the spiral arms are trailing and from the observed projected velocity field (see Sect. 5.3) we conclude that the NE is the near and the SW the far side of the disk. The northern arm of UGC 3995 appears more "open" and diffuse than the southern, which more likely implies tidal disturbance of the galactic disk, rather than being a projection effect.

Table 6 summarizes the measured photometric data for the bulges of both galaxies and the two brightest (non-saturated) stars in the field. We also give the colours for the structure "J" that was described by Keel (1985) as a possible jet from the nucleus of UGC 3995 but, from its aspect and color, it seems to be an unrelated background galaxy.

The contribution of emission lines to broad band images is very small (maximum $\sim 3\%$ in the V band due to the $[OIII]$ emission lines of UGC 3395). Consequently, the colour maps are well representative of the stellar populations. We find that the disks of both galaxies are bluer than the bulges and, although star formation must be going on, the colours are normal for late type spirals.

We have used the IRAF task ELLIPSE to fit the isophotes of UGC 3996, on the B image. In the inner $10''$ the isophotes are approximately circular, with a slight NE-SW elongation in the direction of the spiral arms (see Fig. 14c). Both the ellipticity and position angle increase outwards, as the isophotes start following the bar-like structure.

Assuming an ellipticity ϵ=0.5$\pm$0.1 and a position angle Φ=108$\pm$ 10° from the outer best fitted isophote (μ=22.5 mag arcsec^{-2}), we find an inclination i=60° from the relation cos i = 1-ϵ, or i_0=55° from the relation cos i_0 = $\sqrt{\frac{q^2 - q_0^2}{(1-q_0)^2}}$ (q_0 is taken from Bottinelli et al., 1983, for morphological type T=4 and $q = 1 - \epsilon$). This is comparable to i=64° given by Bicay and Giovanelli (1986). We attribute a morphological type $SAB(bc)$ for UGC 3995 and a medium $SA(s)$ for the companion.

5.2. Reconstructed images and spectroscopy

We reconstructed intensity images in the continuum band 5500-6500 Å and in the principal emission lines and also derived velocity maps. The small field of view ($32''$), compared to the dimensions of the system, precluded us from having both galaxies simultaneously in the field. In Fig. 14c we show the continuum (5500-6500 Å) reconstructed image in negative greyscales with overplotted contours of the reconstructed $[OIII]_{5007}$ intensity image.

The continuum emission is centered on the optical nucleus of UGC 3995 and appears much more extended than the emission line gas, although the emission center coincides in all reconstructed images. The ionized gas, as traced by the $[OIII]_{5007}$ emission line, appears extended around the nucleus, by $\sim 8''$(2.4 kpc) across, in a NW-SE direction that roughly coincides with the bar-like structure seen on the direct images. The $[NII]_{6583}$ line emission is less extended and the H_α line emission is faint and confined to the nuclear regions, with no counterparts of the $[OIII]_{5007}$ emission. Several $H\alpha$ knots are seen at $\sim 14''$-$21''$NW from the nucleus. Comparing the reconstructed with the direct images, we find that these knots must be associated with the eastern spiral arm of the companion galaxy. We label the knots 1-4, from SW to NE. We have extracted a small number of spectra of individual fibers corresponding mainly to the central emission of UGC 3995 and the four emission knots. Fig. 14d shows the nuclear spectrum averaged over two fibres. The most important emission lines are seen here, namely the $H\beta$ and $[OIII]_{4959,5007}$ lines in the spectral range 4800-5400 Å and the $[OI]_{6300}$, $[NII]_{6548,6583}$, $H\alpha$ blend and $[SII]_{6716,6731}$ lines in the range 6370-6870 Å.

Absorption features, such as the $MgI_{5175+5183}$ blend, the $NaID_{5893}$ doublet and the G_{4304} band, were strong in all our spectra and in some cases the $H\beta$ and $H\gamma$ emission lines were obviously contaminated by the underlying absorption. The Balmer absorption equivalent width is of the order of 4 - 4.5 Å which is typical for giant A stars. Consequently, for this object we felt that it was important to correct our spectra for the strong underlying Balmer absorption. For this purpose, we have used the most appropriate of the templates calculated for nuclei of spiral galaxies by Bica (1988), that includes in its predicted ranges the morphological type and luminosity of our galaxy, selected so as to reproduce as best as possible the observed equivalent widths of the various absorption lines that are not contaminated by emission lines. The best template so selected corresponds to a stellar population of solar metallicity with important contribution of young stars, with MgI_{5175} and G_{4304} equivalent widths of the order of 6-7 Å.

The corrections calculated as described above are very important for $H\beta$ and $H\gamma$, of the order of 50% to 60%, due to the faintness of these lines and close to 40% for $H\alpha$. This implies that a slight error in the correction factor for the underlying absorption would affect seriously the resulting emission fluxes. However, judging from the residual spectra after subtraction of the template, we are confident that the uncertainty in the corrected fluxes is less than $\sim 10\%$.
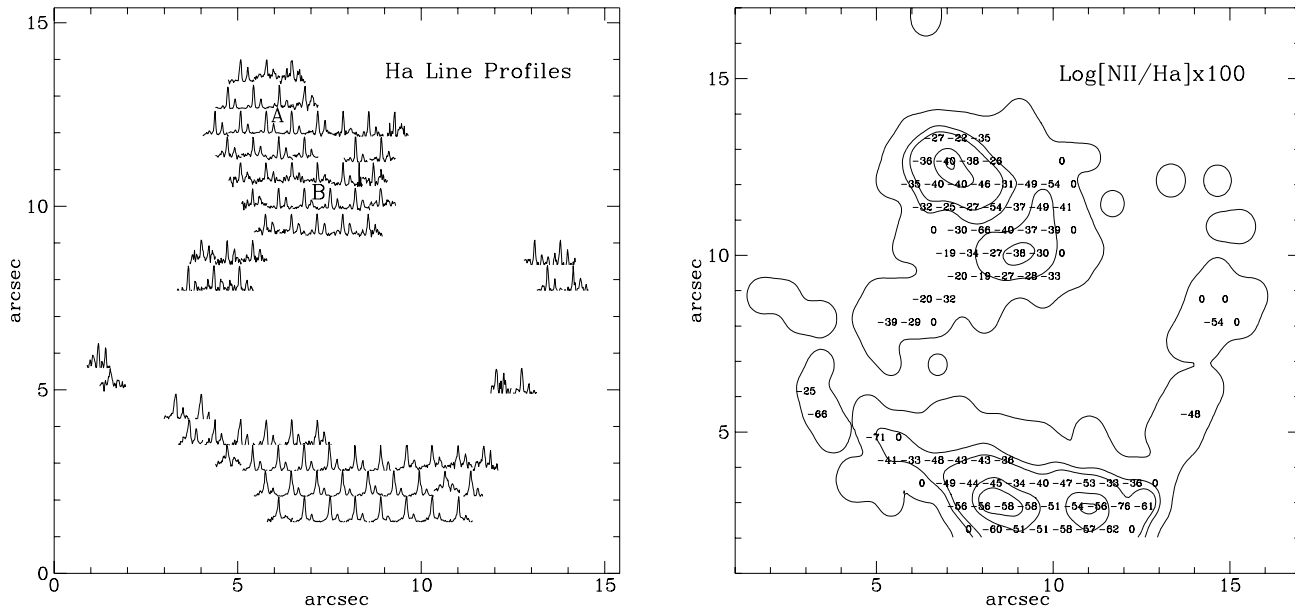
Fig. 12a and b. Spatial distribution of the $H\alpha$ line profiles **a** and of $\mathrm{Log}\frac{[NII]_{6583}}{H_\alpha}\times 100$ **b** throughout UGC 4085. The "centers" of knots A and B are indicated with labels.

After this correction, the $\frac{H_\alpha}{H_\beta}$ ratio was found to be close to the theoretical value of 3.1, implying no significant internal reddening for this object. Consequently, we did not apply any further correction to the observed fluxes.

From 21cm observations, Bothun et al. (1985) and Bottinelli et al. (1990) give a corrected systemic velocity of 4753 km s^{-1} and 4749 km s^{-1} respectively. In order to compare these results with our data, we constructed "global" profiles for three different lines, $[OIII]_{5007}$, (deblended) $H\alpha$ and $NaID_{5893}$, by summing the high S/N individual spectra over the whole galaxy, as for the previous two objects. We have then calculated the midpoint velocity and the barycenter of these global profiles. Within our estimated uncertainties (50 km sec^{-1}) both the midpoint and the barycenter velocities, deduced from the absorption global profile (4751 and 4728 km sec^{-1} respectively), are comparable to the barycenter velocities from the $[OIII]_{5007}$ and $H\alpha$ global profiles (4772 and 4767 km sec^{-1} respectively) and in excellent agreement with the velocities deduced from the 21cm data. On the other hand, the $[OIII]_{5007}$ and $[NII]_{6583}$ midpoint velocities, were affected by the asymmetric line profiles (see next section) and thus are not credible.

In what follows, we adopt a systemic velocity of 4750$\pm$ 50 km s^{-1} (z=0.0158).

5.3. Ionization and kinematics

(a) *Flux ratios*

The spatial distribution of the $[OIII]$(4959,5007)Å and $H\alpha, [NII]$ line profiles, throughout the object, is shown in Fig. 15. We have enlarged the central $(12'')^2$ region, omitting the four $H\alpha$ knots in order to better illustrate the structure on the profiles. The H_α emission remains weak relative to the $[NII]$ lines everywhere except for the central two fibres. A fourth peak bluewards of the $H\alpha$, $[NII]$ blend is visible on a couple of spectra south of the nucleus. Although tempting, it is not confirmed on the spectra of the red grism, so it is most probably an artifact due to the residuals of a cosmic ray in this region of the spectrum.

In Table 7, we list the mean flux ratios calculated within annuli of increasing distance from the nucleus. We give the ratios calculated both before and after correction for the underlying Balmer absorption. We have considered only lines with intensities larger than 3σ above the noise in the adjacent continuum. This resulted in line ratio information for only the central $2''$(0.6 kpc) region. As expected, the line ratio most affected by the correction is $\frac{[OIII]_{5007}}{H_\beta}$. Moreover, the Balmer absorption affects mostly the spectra far from the nucleus, where the gas emission is significantly lower. The large discrepancies in the observed values of $\frac{[NII]_{6583}}{H_\alpha}$ and $\frac{[SII]_{6716+6731}}{H_\alpha}$ with distance from the nucleus disappear in the corrected line ratios, indicating that the applied corrections were appropriate.

From the $\frac{[SII]_{6716}}{[SII]_{6731}}$ line ratio, one can estimate the electron density N_e (Osterbrock 1989). A higher ratio (lower N_e) is expected with increasing distance from the nucleus, but the lines there become also more noisy. Thus, giving more weight to the central values, we find a range of 460 - 200 cm^{-3} for the N_e as we move from the nucleus to the outer regions, assuming an electron temperature of $10000^o K$.

The line ratios within r=1.4$''$(label N) and r=1.4-2.1$''$(no label) from the nucleus are plotted on Fig. 16 symbolized with filled triangles. The large error bars for the circumnuclear region in Fig. 16b are due to the faintness of the $[OI]$ line in this region (we remind that error bars are estimated from the % error in the line fluxes, as described in Sect. 2.) The points fall
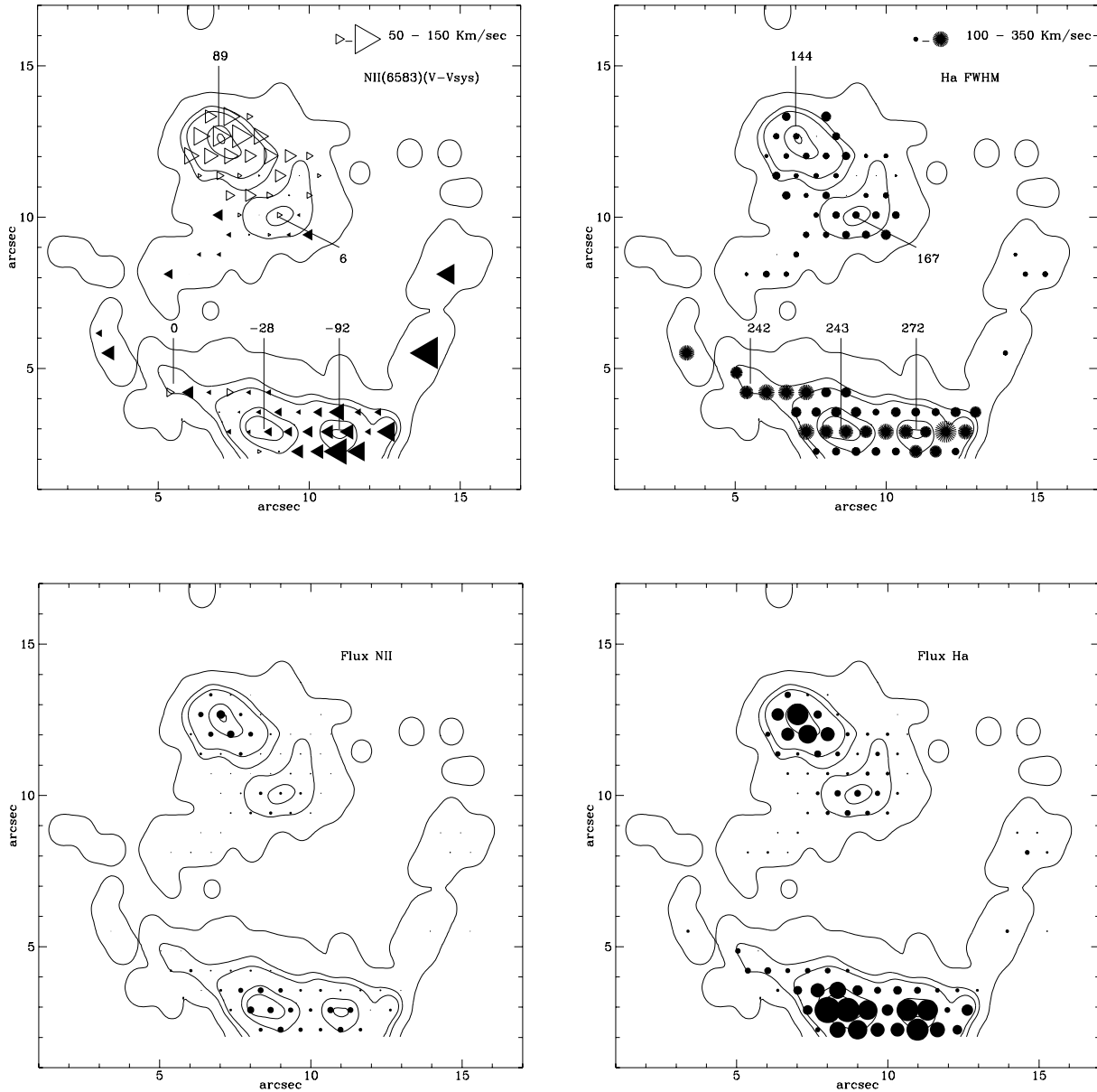
Fig. 13. a Spatial distribution of the $[NII]_{6583}$ line velocities, presented as shifts from the systemic velocity, for UGC 4085. Filled/open triangles denote blue/red shifts respectively. **b** Spatial distribution of the $H\alpha$ line widths. On both diagrams, the scales are shown on the upper right and the numbers indicate velocities and widths measured from the integrated spectra of the five knots. **c** and **d** Spatial distribution of the $[NII]_{6583}$ and $H\alpha$ line emission. The flux ranges up to 1.9×10^{-15} ergs cm^{-2} sec^{-1} for $[NII]$ and 5.8×10^{-15} ergs cm^{-2} sec^{-1} for $H\alpha$. In all four plots, points are overplotted on a contour map of the $H\alpha$ emission.

well within the region assigned to narrow-line AGNs (Veilleux and Osterbrock 1987), where ionization by a central power-law source operates. Another indicator for this is the detection of the $[HeII]_{4686}$ line in the central fibres. We indeed find a mean ratio $\frac{[HeII]_{4686}}{H_\beta} \sim 0.25$, which gives an estimate of the power law spectral index of the ionizing continuum between 912 and 228 ÅÅ (Penston & Fosbury 1978), $\alpha \sim$ -1.5. This is a rather typical value for gas photoionized by a power law-like continuum.

The spectra of the four HII knots are dominated by $H\alpha$ and $[NII]$ emission lines, while no higher ionization lines are

detected. In Table 8 we give the observed line ratios for these emission regions, measured from the integrated spectra that we constructed for each knot. Since no absorption lines were detected in any of these spectra, we applied no corrections to the measured emission line fluxes. By far the brightest is knot 4, although only partially covered by our field. The $\frac{[NII]_{6583}}{H_\alpha}$ line ratios are typical of HII regions for all knots, but the scatter in the $\frac{[SII]_{6716+6731}}{H_\alpha}$ ratio is rather large due to the low S/N of the $[SII]$ lines.
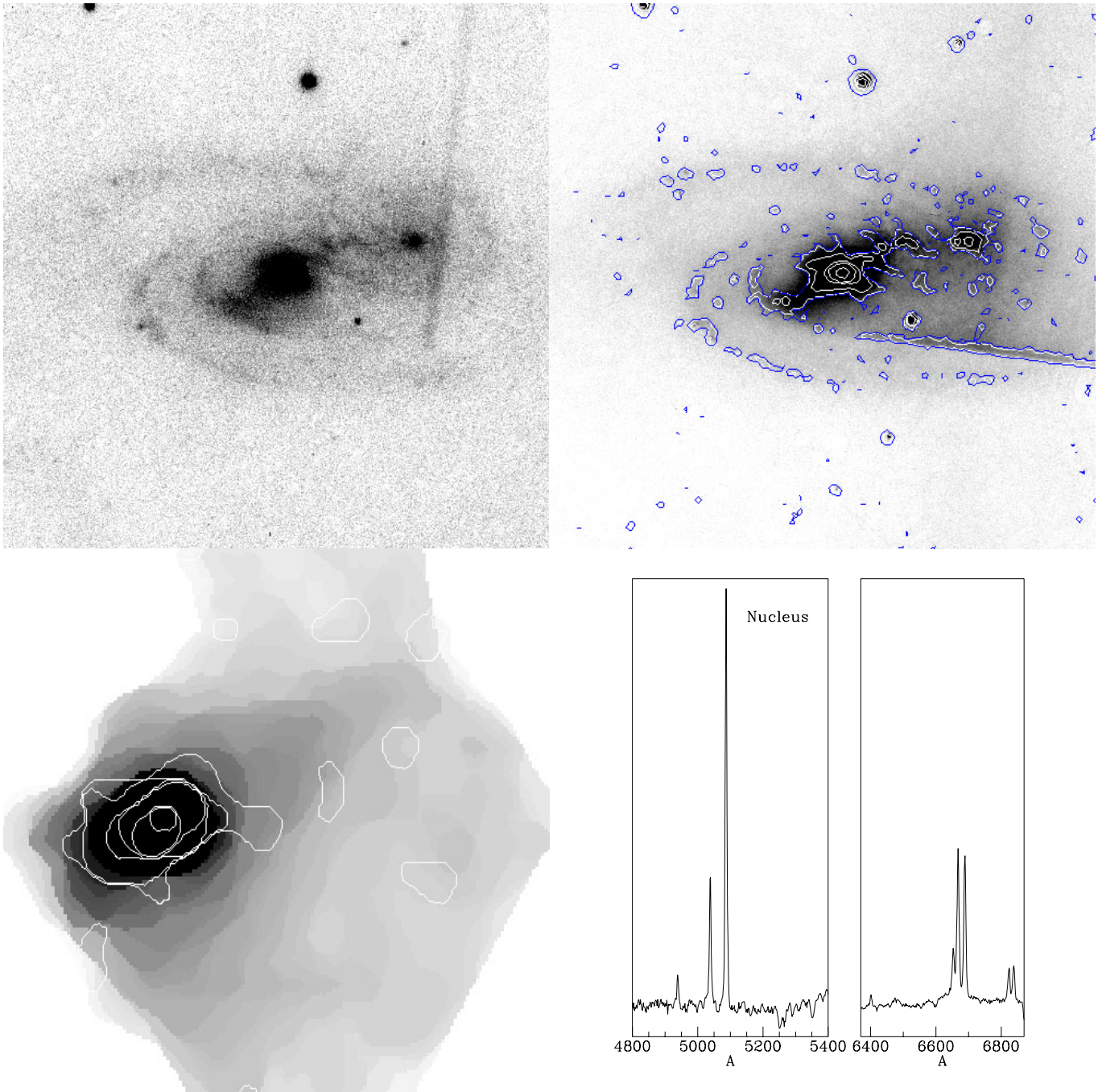
(b) $Velocities$

Fig. 14. a B image of UGC 3995. **b** Contours of the residual R image produced by the technique of unsharp masking, superposed on the original R image.Both images are represented in logarithmic negative greyscales and the field size is $2.1' \times 2.1'$ ($\sim$(37.4×37.4 kpc^2). The linear structures running from S to N in **a** and from E to W in **b** are artifacts, due to the saturation of a nearby star. The orientation is north up and east to the left. **c** Reconstructed continuum (5500-6500 Å) image in negative greyscales, with overplotted contours of the reconstructed $[OIII]_{5007}$ intensity image (both have been smoothed with a median filter). The field of view here is $32'' \times 32''$ ($\sim 9.6 \times 9.6$ kpc ^{2}). **d** Nuclear spectrum averaged over two fibres. For clarity, we only show selected parts of the observed spectral range (see text). The flux scale is arbitrary.
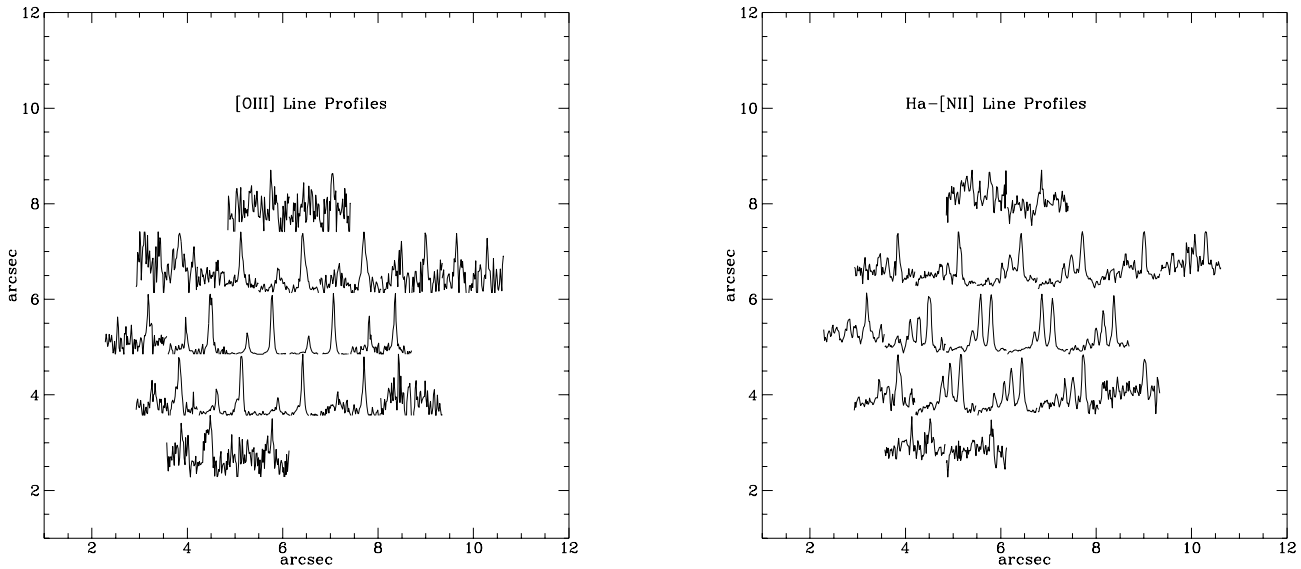
Fig. 15. Spatial distribution of the $[OIII]_{4959,5007}$ and $H\alpha$, $[NII]$ blend line profiles for UGC 3995. For better illustration of the profile structure, only the central $(12'')^2$ region is shown, where emission line from the object was detected.

Table 7. Mean emission line ratios for the gas in UGC 3995

r	$\mathrm{Log}\frac{[OIII]_{5007}}{H_\beta}$	$\mathrm{Log}\frac{[NII]_{6583}}{H_\alpha}$	$\mathrm{Log}\frac{[SII]_{6716+6731}}{H_\alpha}$	$\mathrm{Log}\frac{[OI]_{6300}}{H_\alpha}$	$\frac{[SII]_{6716}}{[SII]_{6731}}$
		Observed	ratios		
Nuclear	1.13	-0.005	-0.34	-1.03	0.97
$1.4''$	1.13	0.02	-0.28	-1.03	0.99
$1.4''$- $2.1''$	1.15	0.17	-0.09	-0.86	1.14
$2.1''$- $3.5''$	-	0.49	-	-	1.28
	Corrected	for	absorption		
Nuclear	0.74	-0.08	-0.41	-1.10	
$1.4''$	0.74	-0.09	-0.39	-1.14	
$1.4''$- $2.1''$	0.77	0.002	-0.27	-1.00	
$2.1''$- $3.5''$	-	0.08	-	-	

The first column indicates distance from the nucleus. In the second table the Balmer fluxes were corrected for underlying absorption.

In Figs. 17a-c we present the projected velocity field for UGC 3995 as deduced from the $[OIII]_{5007}$, $[NII]_{6583}$ and H_α lines respectively. These represent mean velocities measured from Gaussian fits of the line profiles. For $[OIII]_{5007}$ we also measured the peak velocities (at the 80% intensity level) and found that they have a similar distribution. Velocities are plotted only when the line intensities exceed 3σ above the noise level of the adjacent continuum and this was the case within only the central 10 arcsec.

The interesting feature here is that the kinematic axis orientation is not the same for all the emission lines. On the $[OIII]_{5007}$ velocity map, the kinematic axis of nodes follows approximately the photometric "major" axis deduced from the outer (radius $\gtrsim 10''$) isophotes (see 5.1). However, the kinematic axes on the $[NII]_{6583}$ and H_α velocity maps rotate progressively towards the NE, from PA$\sim 64^o$ to $\sim 54^o$ respectively, following the inner isophotal twisting that we found on the direct images (Sect. 5.1). Distortions on the isocontours are visible, but may not be real, taking into account the large error bars

of our measurements ($\pm$ 50 km sec^{-1}). On the other hand, the $[OIII]$ profile substructure seen in Fig. 15a is certainly real. The $[OIII]_{5007}$ lines become asymmetric further from the nucleus, in the same direction as the extended line emission. Fig. 17d shows the distribution of AI_{20}, the asymmetry index at the 20% intensity level (as defined in Paper I), that ranges from +0.42 (blue wing) in the SE to -0.35 (red wing) to the NW.

Another way to see the tendency of the kinematic axis to rotate between the $[OIII]_{5007}$, $[NII]_{6583}$ and H_α lines from 110° to smaller position angles is to plot the radial velocity curves for the three lines along various directions. In Fig. 17e, we plot the velocity curves along the photometric major axis (PA=110°), where the $[OIII]_{5007}$ line reaches a maximum velocity amplitude ~ 250 km sec^{-1}. In Fig. 17f we plot the same curves but along PA=60°, where the maximum amplitude ~ 150 km sec^{-1} is reached for the H_α and $[NII]_{6583}$ lines. These results will be further discussed in the next section. In Table 8 we list the measured "mean" H_α velocities for the four emission knots (which are also plotted in Figs. 17b and c for the knots 2 and 3). Within
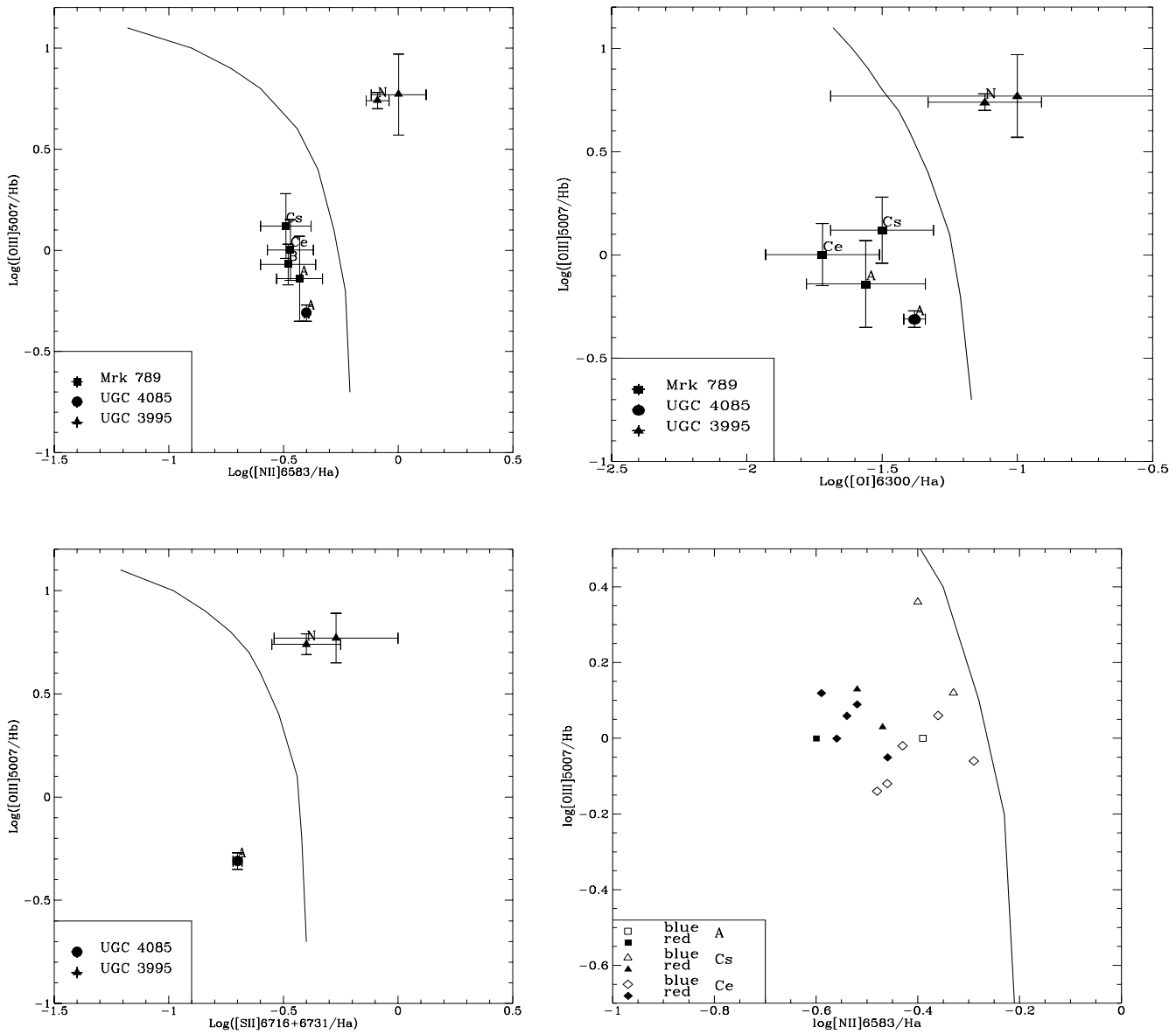
Fig. 16. Diagnostic line ratio diagrams for Mkn 789 (squares), UGC 4085 (circles) and UGC 3995 (triangles). The labels represent the various regions identified on each object and for UGC 3995, N represents the nuclear spectrum (see text). The line divides AGNs from HII region-like objects (Veilleux & Osterbrock 1987).

the uncertainty of the measurements, there is no appreciable velocity shift between UGC 3995 and the knots. Keel (1985) has reported a projected velocity difference of 400 km sec^{-1} between the nuclei of the two galaxies. Consequently, our finding would either mean that the four knots belong to UGC 3995 or, if they indeed belong to the spiral arm of the companion, the gas must have been captured by the main galaxy during the interaction process.

The line widths are measured at half maximum line intensity and deconvolved with the sky line widths as for the previous objects. The $[OIII]_{5007}$ lines are narrow, 250-300$\pm$ 50 km sec^{-1}, near the nucleus increasing to $\sim$ 500 km sec^{-1} in the outer regions due to the substructure of the profiles. For the H_α and

Table 8. Measured parameters for the HII knots in UGC 3995

Knot	Log[$\frac{[NII]_{6583}}{H\alpha}$]	Log[$\frac{[SII]_{6716+6731}}{H\alpha}$]	$V_{H\alpha}$ (km sec^{-1})	$FWHM_{H\alpha}$ (km sec^{-1})
1	-0.68	–	4768	218
2	-0.51	-0.41	4741	107
3	-0.53	-0.65	4730	204_u
4	-0.78	-0.21	4782	217_u

The index u denotes unresolved lines

$[NII]_{6583}$ lines, the widths are evenly distributed, from $\sim$ 300 to 400 $\pm$ 50 km sec^{-1}, with distance from the nucleus.
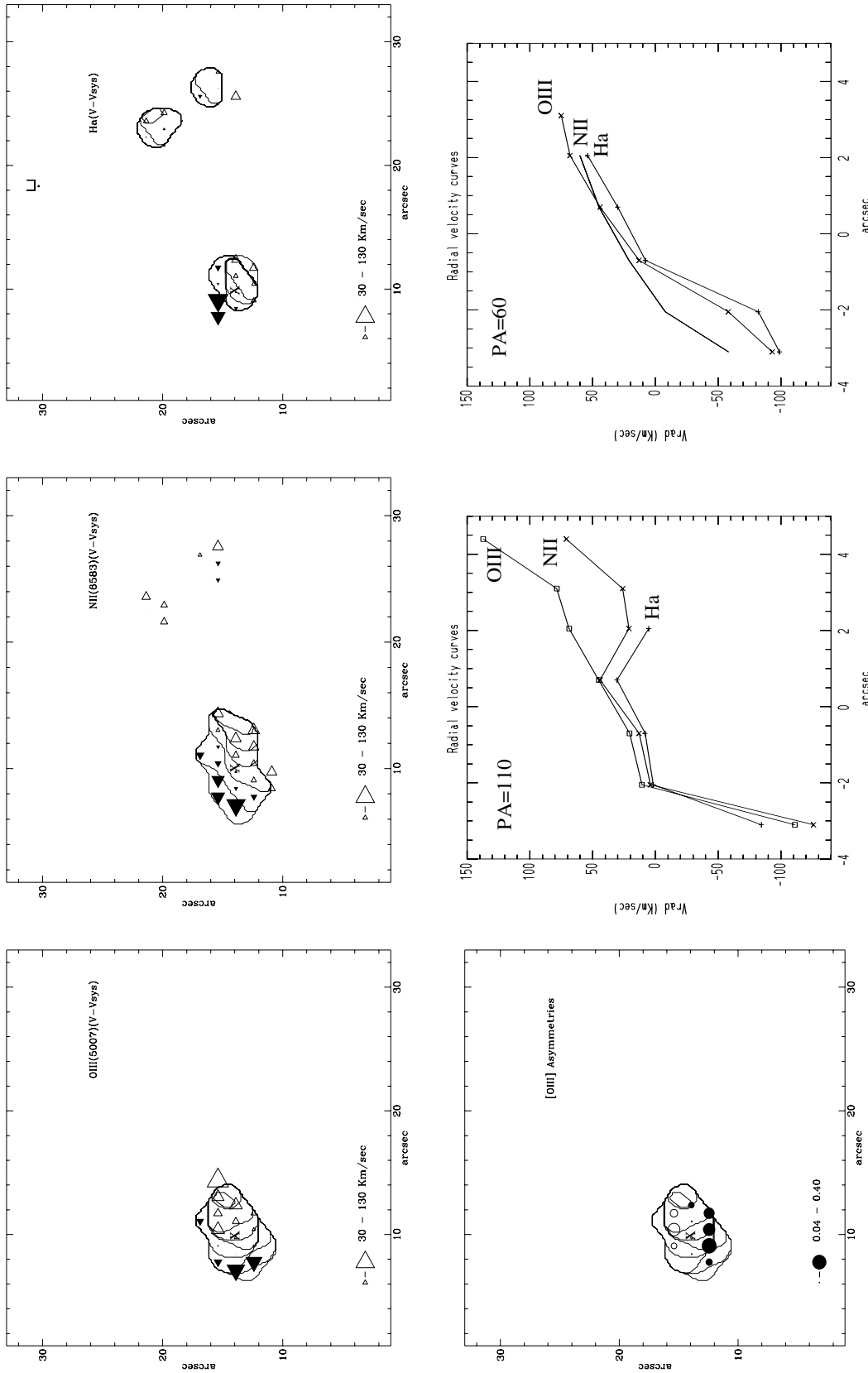
Fig. 17a–f. Spatial distribution of the $[OIII]_{5007}$ (**a**), $[NII]_{6583}$ (**b**), H_α (**c**) velocities and $[OIII]_{5007}$ line asymmetries (**d**), superposed on the respective isovelocity contours for UGC 3995. Filled/open triangles denote blue/red shifts from the systemic velocity, respectively. In **d** filled/open circles denote blue/red asymmetries respectively, presented as a 20% level asymmetry index AI_{20} (see text). In all diagrams, the size of the symbols scales with the plotted parameter values, the scale is shown on the lower left side. The position of the optical nucleus is indicated by an "X". **e** and **f** Radial velocity curves for the three lines, along PA∼ 110° and 60° respectively (see text).

6. Discussion

In Table 9 we list the most important observed and derived properties of the four systems studied so far (Paper I and present paper) i.e., Mkn 463, Mkn 789, UGC 4085 and UGC 3995.

6.1. Kinematic features

First, we describe the main kinematic features for each object and some other parameters characterizing the velocity field:

(1a) the "systemic" velocity derived from the emission line gas in this study

(1b) the systemic velocity derived from HI observations (references are given in the table footnotes)

(1c) characterization of the general velocity field and the largest kinematic disturbance (if present)

(1d) the maximum (radial) velocity amplitude over the whole extent of the object (a "shear" type measure)

(1e) the maximum line width measured at the half maximum intensity of the gaussian fit (a measure of the velocity dispersion) and

(1f) the velocity difference between the two main nuclei or "hotspots" for each object.

In all cases, the velocity uncertainties are ± 50 km sec^{-1}.

6.1.1. Mkn 789

As we have seen in 3.3, the diagnostic diagrams clearly suggest that the line emission from all regions of Mkn 789 is consistent with gas photoionized by hot stars, with the line splitting region which has the highest emission line surface brightness to show the highest ionization. The rapid increase of the emission line surface brightness, especially for the higher ionization lines, at the edges of the line splitting region together with the increase in the $[NII]$ line widths and the sharp edge appearance of the structure C in the optical images, all suggest anomalous physical conditions in this region. Heckman et al (1990) argued that double-peaked profiles together with strong narrow emission lines in FIRGs are signatures of gas outflow driven by a central starburst. The presence of shocks driven into the medium by the outflow are however not indicated by the line ratios, which are in this region (as everywhere else in this object) typical for gas photoionized by hot stars (Evans & Dopita 1985, Mc Call et al. 1985). The relative increase of $\frac{[OIII]_{5007}}{H_\beta}$ and $\frac{[OI]_{6300}}{H_\alpha}$ can be explained within the range of parameters predicted by classical HII region models, with a larger ionization parameter U due to the younger massive stellar population in the region C. Both the $\frac{[NII]_{6583}}{H_\alpha}$ and $\frac{[OI]_{6300}}{H_\alpha}$ ratios are too small to indicate additional shock heating.

If the line splitting in Mkn 789 is interpreted as gas outflow then, in a biconical morphology, line emission from the central region of C (labelled Ce) would be expected to come from the near-side of the cone while, on the overall fainter SW extension (labelled Cs), emission would come from the far cone side. From Fig. 7 we see that the blue component is closer to the systemic velocity V_0 (shifted by 100-200 $\pm$ 50 km sec^{-1}) compared to the red component (shifted by 500-600 $\pm$ 50 km sec^{-1}), while the

opposite effect would be expected for a simple conic geometry for the outflow (Heckman et al. 1990). From our images (figures 1 and 2) as well as the HST R-band image (Gorjian 1995), there is no evidence for such a geometry: the line-splitting region appears as a patchy, elongated, rather linear structure. The large extinction within this object prevents us from determining the position of the galactic nucleus (nuclei). Although outflow may well be occuring, it is not possible to deduce its geometry from the present data.

In Sect. 3.3 we have shown that outside the line splitting region the line-of-sight velocity distribution is flat. It is interesting that Keel (1993), studying the kinematics of interacting spirals, finds that the largest star formation rates occur in galaxies which have "flat" velocity curves, with overall velocity amplitudes less than 50 km sec^{-1}. The almost complete absence of any radial component outside of the split region in Mkn 789 indicates that strong tidal forces may operate, producing violent motions outside of the galaxy plane that give to the system its patchy appearance and annulate any signatures of rotational motion in the parent systems.

The $NaID_{5893}$ absorption line is mostly detectable outside the emission regions, where it is not efficiently diluted by the strong continuum and line emission. It was also detected in two spectra from regions A and B but not observed in region C. The velocity field deduced from this doublet is evenly distributed throughout the object (except for the region C), in the range ~ 150-200 ± 50 km sec^{-1} above the systemic velocity that is in rough agreement with the $H\alpha$ velocity field. Because there is no detectable MgI line absorption observed throughout the object, most of the NaI absorption must have interstellar origin.

6.1.2. UGC 4085

The nature of the two central emission knots in this object is controversial. Knot A, the brightest and bluest of them, is elongated and resolved in our broad band images with dimensions of the order of 1 arcsec. The second knot B is visible on the V and especially on the R band image and appears also elongated. The apparent separation between the two knots is only $\sim$ 3.3 arcsec ($\sim$ 1.5 kpc). Whether they belong to the same central structure, that is partly obscured by dust associated with the bar, is unclear.

The kinematic information further helps to constrain the nature of the two knots. The generally smooth velocity field of the ionized gas (Sect. 4.3) and the absence of any optical tidal features reminiscent of a violent interaction seem to exclude the possibility of these being two different stellar systems in the process of merging . Absorption features, mainly the $NaID_{5893}$, were detected in only a few spectra on the bar-like structure around knot B and in two spectra on knot A, with equivalent widths of the order of 4-5 Å. Velocities deduced from these lines follow the emission line velocity field. The location of knot B close to the kinematic center of the galaxy gives further support to the idea that this might be the location of the galactic nucleus that remains embedded in large amounts of dust, as its very red colours (4.1), large Balmer decrement and relative

Table 9. Miscellaneous Observed and Derived Properties for all Four Systems

Properties	Mkn 463	Mkn 789	UGC 4085	UGC 3995
(1) Kinematic features				
(a) *General Velocity field*	No radial component Sharp gradient - radio jet	No radial component Line splitting	Smooth retrograde -	Smooth prograde Distortions
(b) V_{gas}(km s^{-1})[1]	15209	9390	7350	4750
(c) V_{HI}(km s^{-1})	15230$\pm$ 30[2]	9305$\pm$ 50[3]	-	4749$\pm$ 5[4]
(d) ΔV_{max}(km s^{-1})	500	700	300	250
(e) ΔW_{max}(km s^{-1})	800	900	350	500
(f) ΔV_n(km s^{-1})	100	0	80	400
(2) Line emission				
(a) $Log(L_{H\alpha t})(L_\odot)$	8.66	8.82	7.64	6.54
(b) $Log(SB_{H\alpha t})(\frac{L_\odot}{kpc^2})$	6.73 (84.79)	7.80 (10.45)	6.79 (7.10)	6.19 (2.22)
(c) $Log(SB_{H\alpha n})(\frac{L_\odot}{kpc^2})$	7.84 E (2.5)	8.32 A (1.03)	7.18 A (0.24)	5.85 (0.28)
	6.47 W (2.5)	7.85 B (0.52)	6.71 B (0.32)	
		8.15 C (1.03)		
(3) Morphological properties				
(a) S(kpc)	4.0	2.6	1.5	8.8
(b) D(kpc)	34.2	30.1	31.1	41.0
(c) $Log(A)$(kpc^2)	3.37	3.36	3.32	3.42
(d) 1-$\frac{b}{a}$ [7]	0.37	0.25	0.40	0.50
(e) $PA(^o)$ [7]	83	70	74	108
(4) Blue luminosity				
(a) $Log(L_{Bt})(L_\odot)$ [9]	(10.58)	10.17	10.09	(10.12)
(b) $Log(L_{Bn})(L_\odot)$ [8]	9.58 E	9.57 A	8.73 A	9.30
	9.21 W	9.07 B	8.40 B	
(5) IR properties				
(a) $Log(MFIR)$(erg cm^{-2} s^{-1})	-9.43	-9.59	-9.88	-9.87
(b) $Log(L_{FIR})(L_\odot)$	11.26	11.07	10.60	9.98
(c) $\alpha(25,60)$	-0.35	-1.90	-2.20	-0.70
(d) $\alpha(60,100)$	0.30	-0.52	-1.68	-2.21
(e) $\alpha(V,60)$	-1.72	-1.39	-1.06	-1.15
(f) $IRCI$	3.09	1.54	0.39	1.8
(6) Star Formation				
(a) $SFR_{H\alpha t}(\frac{M_\odot}{yr})$	12.23	17.87	1.17	0.09
(b) $SFR_{FIR}(\frac{M_\odot}{yr})$	89.96	58.24	19.56	4.68
(c) $\frac{SFR_{FIR}}{SFR_{H\alpha}}$	7.4	3.3	16.7	52
(7) $Log(M_{HI})(M_\odot)$	9.29[5]	9.57[3]	-	9.83[4]

H_o = 75 km sec^{-1} Mpc^{-1}

[1] From the present study. Uncertainties are $\pm$ 50 km s^{-1}

[2] From Hutchings et al. (1987)

[3] From Martin et al. (1991)

[4] From Bottinelli et al. (1990)

[5] Calculated from HI data published by Hutchings et al. (1987)

importance of the continuum/line emission (4.2) suggest. The smooth velocity increase from knot B towards knot A in the sense of disk rotation supports the interpretation that knot A might be a giant HII region, associated with the far-side spiral arm.

The present optical data is thus not sufficient to infer the position of the galactic nucleus; near IR photometric observations might help to resolve this issue. Deep spectroscopy would be useful in order to reveal the kinematics of the *stellar* component. This situation resembles that of NGC 520, with two central

emission peaks detected in the near IR (Standford & Balcells 1990). Hibbard & Van Gorkom (1996) recently found that the atomic gas velocity field resembles a single rotating disk but stellar kinematics show that the two nuclei rotate around each other (in the same sense as the disk), thus confirming that NGC 520 is a merger of two disk galaxies. Consequently, we can not exclude at this stage the merger nature for UGC 4085 based solely on the kinematics of the disk hot gas and on the optical appearance of the system.

6.1.3. UGC 3995

The emission line data for UGC 3995 (5.3) indicate that this galaxy harbours a Seyfert nucleus. The low derived electron densities and the position of this galaxy on the diagnostic diagrams suggest it to be a relatively low ionization AGN. We have seen that, as we move progressively outwards, the isophotal axis rotates towards larger position angles, in the same way as the kinematic axis defined by the $H\alpha$, $[NII]$ and $[OIII]$ velocity fields, respectively (Sect. 5.3). This likely indicates that the H_α and $[NII]$ lines trace the gas in the inner regions while the highly ionized gas is extended along the bar/bridge-like structure identified in the starlight (Sect. 5.1). Often, similar asymmetric morphology of the extended gas is interpreted in terms of ionization cones with their apex on the nucleus (e.g. Wilson & Tsvetanov 1994, Wilson 1996). We have also found substructure in the $[OIII]_{5007}$ line profiles (Fig. 15a and 17d) further from the nucleus, along the direction of the extended emission. We interpret this as a high velocity component, with a maximum blue velocity shift of $\sim 550\pm 50$ km sec^{-1} to the SE (far side) and somewhat smaller to the NW (near side). This is consistent with gas inflow along the bar and might well be the mechanism for fueling the active nucleus. We need higher resolution spectra to disentangle the "cone" component from the $[OIII]$ disk emission and higher signal to noise data to trace this component further out.

Simulations show that collisions between gas-rich galaxies will always drive large scale in/out flows perpendicular to the disk plane, of the order of few hundred km sec^{-1}. The flowing material develops complicate shock structures that might lead to enhanced star formation, stellar rings or half rings etc, depending on the assumed geometry of the encounter (e.g. Lamb et al. 1994). If the inflowing gas loses most of its angular momentum in some way, it will fall into the inner few kpc region, feeding directly a pre-existing black hole or forming one through a central star formation. Bar formation provides an efficient mechanism for dissipating the gas angular momentum through gravitational torques due to phase differences between the gaseous and stellar bars (Quillen et al. 1995, Barnes & Hernquist 1996). Numerical simulations show that colliding disk galaxies often develop bars due to the strong tidal forces exerted at closest passage (e.g. Barnes & Hernquist 1996). Consequently, gas inflow observed at small scales (of the order of ~ 1 kpc) might be indicating the activation mechanism of the central engine and this could indeed be the case of UGC 3995. But in the case of the double nucleus system Mkn 463, that we presented in Paper I, the sharp blueshifted component that we observe within 1.8 kpc from the Seyfert nucleus is interpreted in terms of bowshocks driven by the radio jet into the ambient gas rather than being directly related to the merger. It is indeed unlikely that the observed gas dynamics in mergers provide direct clues to the merging process, as hydrodynamic processes can be much more important/energetic and thus dominate the kinematics of the system, at least in the central regions. Winds from starbursts (case of Mkn 789) and AGN and the coupling between radio emission and ambient material (case of Mkn 463) can generate velocities

of many hundreds to thousands km sec^{-1}. On the other hand, the motions that a merger can generate, taking into account factors such as dissipation, inefficient coupling and confusing ambient gas, result in much smaller velocities generally. Our data presented so far support this point of view.

6.2. The "Superwind" in Mkn 789

Our observations have revealed a region of line splitting within the galaxy Mkn 789. One possible explanation for such line splitting is that the starburst within Mkn 789 is driving a large scale wind ("superwind"). Finding evidence for a superwind is not totally unexpected. Recent results (Lehnert & Heckman 1996; Heckman, Armus, & Miley 1990) have shown that starburst galaxies with large IR luminosities ($L_{IR} \gtrsim 10^{44}$ erg s^{-1}), large IR excesses ($L_{IR}/L_B \gtrsim 2$) and warm far-IR colors ($S_{60\mu m}/S_{100\mu m} \gtrsim 0.5$) have properties consistent with such galaxies driving superwinds. Mkn 789 meets all of these criteria. In this regard, it is interesting to note that while UGC 4085 was also IR selected and does have an HII-region-like nuclear spectrum it does not meet all the criteria for driving a wind (L_{IR} and L_{IR}/L_B do meet the criteria, but the $S_{60\mu m}/S_{100\mu m}$ is less than 0.5).

The theory of superwinds has been well-studied (e.g., Chevalier and Clegg 1985; Tomisaka & Ikeuchi 1988; Suchkov et al. 1994; 1996). Theory suggests that a superwind results when the energy injection rate is high enough to excavate a cavity at the center of a starburst. The collisions of numerous supernova remnants and stellar winds convert their kinetic energy into thermal energy, with initially little energy being lost to radiation due to the high temperatures and low densities within the cavity. In this cavity, the hot fluid has a sound speed much greater than the local escape velocity and a pressure much higher than the ambient interstellar medium and thus will expand (mainly along the direction with the steepest pressure gradient), as a superbubble into the host galaxy's interstellar medium. As the bubble expands it will sweep-up the ambient medium, which collapses due to radiative cooling into a thin shell. The shell eventually breaks up into clumps due to dynamical and/or thermal processes (Rozyczka 1985). After the break-up of the shell the bubble "blows-out" and now the wind may be described as the superwind flowing out of the plane of the galaxy.

To gauge whether it is possible for the star-formation within Mrk 789 to power a superwind, we need to estimate the rate at which mechanical energy and momentum are being injected. Since the optical emission line gas only traces a small amount of the mass involved in a superwind (see Heckman, Lehnert, & Armus 1993), in what follows we will only make order of magnitude estimates. Adopting a velocity of 500 km s^{-1} (which represents the "typical" magnitude of the velocity separation over the region of split lines) and a radius of 2.4 kpc ($\approx$4" at the redshift of Mrk 789 in our adopted cosmology), we estimate a dynamical time $t_{dyn} \sim r/v \sim 5\times 10^6$ yrs. We estimate that the luminosity of Hα emission over the region of split lines is about 10^{42} ergs s^{-1} or about 60% of the total Hα luminosity. The mass responsible for the Hα emission can be estimated assuming case

B conditions, $T_e = 10^4$ K and $L_{H\alpha} = 10^{42}$ ergs s^{-1}, which give a total Hα emitting gas mass of 8×10^7 N_e^{-1} $M_\odot$. We note that assuming that the gas is photoionized instead of shock heated does not affect the mass estimate greatly, since in shocked gas most of the line emission due to hydrogen is recombination emission and not collisionally excited line emission (Dopita & Sutherland 1995b). We do not have an idea of the density of the emission line gas ([SII] was just outside of our band pass). If we adopt 100 cm^{-3} as the density of the line emitting clouds (approximately the low density limit of the [SII] lines, which is likely to be correct within a factor of few for this starburst at these radii; see Lehnert & Heckman 1996), then we have M$\sim 8 \times 10^5$ $M_\odot$. Using this mass, the typical magnitude of the line splitting ($\Delta V = 500$ km s^{-1}) and the typical velocity dispersion of the gas ($\sigma \sim$ FWHM/1.67$\sim$450/1.67), we have $E_{kin} \sim M \times (\Delta V^2 + \sigma^2) \sim 10^{55}$ ergs. The rate of energy injection is then dE/dt$\sim E_{kin}/t_{dyn} \sim 10^{41}$ ergs s^{-1}.

Does the stellar population of Mrk 789 have a sufficient energy injection rate to drive a superwind? We estimated that the star formation rate of Mrk 789 is of-order $20 - 60$ $M_\odot$ yr^{-1} (where the range is the difference in using $L_{H\alpha}$ or L_{FIR} to estimate the rate). Models of Leitherer & Heckman (1995) suggest that such a rate of star-formation would provide a mechanical energy injection rate of about 10^{43} ergs s^{-1} from supernovae and stellar winds after a few $\times 10^7$ years. The implied total amount of mechanical energy injected over that time is about $10^{57.5}$ ergs. This should be compared with the total energy and injection rate estimated above, of $E_{kin} \approx 10^{55}$ ergs and dE/dt$\sim 10^{41}$ ergs s^{-1}. It thus appears that the energetics of the starburst are capable of driving the gas motions that we observe. In addition, while we cannot accurately measure the age of the starburst in Mkn 789, starbursts similar to Mkn 789 typically have had their ages estimated to be $\sim 10^{7-8}$ yrs (e.g., Rieke et al. 1980; Bernloehr 1992; 1993). This implies that it is likely that Mkn 789 has had sufficient time to generate line splitting over a region with a radius of 2.4 kpc.

A shock with a speed similar to the magnitude of the line splitting would produce a luminosity of $L_{H\alpha}$ (shock) $= 3 \times 10^{34}$ $n_a A (V_s/500)$ ergs s^{-1} (Dopita & Sutherland 1995a, Binette et al. 1985). Assuming a preshock density, $n_a = 1$ cm^{-3}, a shock velocity of 500 km s^{-1} and an area of the shocked gas of 3" $\times$ 5" which is A$=5.4 \times 10^6$ pc^2, gives a shock luminosity of about 2×10^{41} ergs s^{-1}. This is only about 20% of the total Hα luminosity we observed over the region with split emission lines. From this estimate, we conclude that it is unlikely that shock heating dominates the extended emission line gas. The result is not surprising considering that the mechanical energy of a starburst is of-order few to 10% of the total ionizing luminosity for continuous star formation (Leitherer & Heckman 1995). Consequently we would not expect shock heating to dominate the large scale emission line luminosity and thus the emission line ratios. This is in agreement with the fact that we did not find the emission line ratios in the extended gas to be completely consistent with shock heating (Fig 8c and f). Only the most extreme line ratios observed in the region of split lines are consistent with shock heating (e.g., Dopita & Sutherland 1995b).

6.3. Line emission

In Table 9 are also listed:

(2a) the log of the "total" $H\alpha$ luminosity across the region covered with SILFID.

(2b) the log of the "total" $H\alpha$ surface brightness; the covered projected area is given within parentheses in kpc^2.

(2c) the log of the "nuclear" $H\alpha$ surface brightness; the nuclear projected area is given within parentheses in kpc^2.

The nuclear luminosities listed in Table 9 are derived as follows: For each object we derived a point spread function (PSF) for the B image using the stars in the frame. This was centered and scaled to the maximum intensity pixel of each emission "knot". The area inside which the (total) B flux of the knot equals the B flux of a point source at the same position, was taken to define the extent of the knot over which we subsequently sum the spectra of individual fibres. For the nuclear "knots" this is a measure of the equivalent nuclear flux. Using this method we have measured "nuclear" fluxes for the E and W nuclei of Mkn 463, for the structures A and B of Mkn 789 and UGC 4085 and for the single nucleus of UGC 3995. In order to compare those to the luminosity of structure C in Mkn 789, we have summed the flux in this region over several fibres, so that the final area equals that used for region A.

In Mkn 789, the total H_α luminosity for each of the emitting regions corresponds to the high end of the composite HII region luminosity function given by Hodge et al. (1989). The region C has a much larger luminosity compared to some of the well known HII regions such as 30 Dor (by $\sim$ 6 orders of magnitude) and N5471 (by $\sim$ 3 orders of magnitude). However, the dimensions of the structures in Mkn 789 are much larger compared to the mean size of HII regions. The H_α $surface$ $brightness$ (luminosity per surface area) of C compares with that of the sum of the brightest HII regions in, for instance, UGC A86 and EGB 0427+63, two galaxies in the Local Group (Hodge & Miller 1995).

In UGC 4085 it is likely that knot A is a circumnuclear giant HII region. Knot B could be the bulge of the galaxy, heavily obscured by dust, but it also appears knotty on the H_α intensity image (Fig.10c) and on the continuum map (Fig.10b). Consequently, knot B might be another HII region associated with the near-side spiral arm that confuses any signs of the heavily reddened galactic nucleus that might be located behind it. This interpretation seems to be supported also by the low overall ionization of knot B. We find the H_α luminosity of knot A (Table 9a) to be larger than the luminosity of 30 Dor but comparable to that of N5471. The H_α surface brightness of knot B, although lower by $\sim$ 3 orders of magnitude than the equivalent of region C in Mkn 789, is comparable to the surface brightness of the largest HII regions in the Local Group dwarf galaxies (Hodge & Miller 1995).

6.4. Morphology and blue luminosities

On the direct images we fit the outer isophotes of each object to measure the following parameters listed in Table 9:

(3a) the projected separation between the two main nuclei or "hotspots".

(3b) the diameter of the major axis, as measured on the outer isophotes that correspond to surface brightness: 24.7 mag arcsec^{-2} for Mkn 463, 24.2 mag arcsec^{-2} for Mkn 789 and UGC 4085 and 23.5 mag arcsec^{-2} for UGC 3995.

(3c) the log of the projected area (πab) corresponding to the same isophotal levels as in (3b)

(3d,e) the ellipticity and position angle calculated from the best fitting ellipse to the isophote corresponding to the 3σ level above the sky background.

With the exception of UGC 3995, it is difficult to obtain an accurate surface brightness profile, since for the other systems the starlight is clumped in more than one knot in the central (few kpc) regions and strongly absorbed by dust lanes located throughout the main body. Consequently, we have obtained ellipticities and position angles from the outer isophotes of each system, that correspond to a mean intensity of $\sim 3\sigma$ of the sky noise level. The corresponding projection angles found for UGC 4085 and UGC 3995 (53° and 60° respectively) represent their true inclinations, while this is not the case for Mkn 463 and Mkn 789 which are most likely seen face-on.

Next in Table 9 we list:

(4a) the log of the blue luminosity for the two main nuclear emitting regions in each object, after correction for the emission line contribution.

(4b) the log of the total blue luminosity.

In both cases, L_B is calculated from the B magnitude through the relation:

flux $f_B = 10^{-0.4B-8.17}$ at λ=4400 Å.

The blue luminosity, L_B, is an indication of the luminous mass corresponding to the relatively old stellar galaxy population. This quantity is sensitive to the galaxy size and to the amount of dust obscuration.

We find that the two Markarian galaxies, which are the advanced mergers in our small "sample", have larger total blue luminosities than the other two objects, although the total projected size is comparable for all four galaxies (line (3c)). This is expected since these are objects selected to have UV/B excess and moreover they contain two stellar systems.

6.5. IR properties and comparisons to other samples

The next rows in the table describe the infrared properties of our objects. These are derived from the coadded IR fluxes in the four IRAS bands:

(5a) the total (1-100 μm) $MFIR$ flux in logarithmic units of ergs cm^{-2} sec^{-1}, derived from the relation

$MFIR = 10^{-11} (20 f_{12} + 10 f_{25} + 3.25 f_{60} + 1.26 f_{100})$

(Keel et al. 1994)

(5b) the logarithm of the 60-100 μm far-IR luminosity, defined from the relation

$FIR = 1.26 \; 10^{-11} (2.58 f_{60} + f_{100})$ R

(Helou et al. 1988, in ergs cm^{-2} sec^{-1}), R being a correction factor for the flux missed due to $\lambda \gtrsim 100\mu$m, taken from Lonsdale et al. (1985), assuming a power law ν^1 for the dust

emissivity. In both relations, the flux densities f_{12}-f_{100} are expressed in Jy.

For a normal galaxy, the L_{FIR} scales with L_B and with the galaxy size, while for galaxies that show some kind of activity (starburst, AGN) there is an excess FIR-to-blue luminosity that is due to the active star formation and/or to the presence of an active nucleus. The ratio L_{FIR}/L_B has often been used as a measure of the young/old stellar population dominance, but this ratio is sensitive to the different area sizes that the L_{FIR} and L_B arise from and to dust obscuration.

The IR colours, on the other hand, give a direct comparison between the various dust components and are unaffected by the parent galaxy sizes or luminosities, although they might still be affected by their dust content. In Table 9 we list the various colour indices:

(5c) α(25-60)=2.63 Log($\frac{f_{25}}{f_{60}}$)

(5d) α(60-100)=4.51 Log($\frac{f_{60}}{f_{100}}$)

(5e) α(V,60)=0.49 Log($\frac{f_V}{f_{60}}$)

(5f) IRCI=$[(\alpha(25,60)+2.48)^2+(\alpha(60,100)+1.94)^2]^{1/2}$

The f_{60}/f_{100} flux ratio is commonly used as an indicator of warm dust that is associated with current star formation, but it can be also affected by the cooler ISRF (interstellar radiation field) component. The f_{12}/f_{25} ratio on the other hand should be a better indicator of the truly warm dust component and has been found to vary between quiescent and star forming galaxies (Keel 1993, Mazzarella et al. 1991). Heating of the dust by an active nucleus, can produce an excess radiation at 25μm. Observational evidence for this is the segregation of Seyfert nuclei on IR colour-colour diagrams (Miley et al. 1985, De Grijp et al. 1987) and the tight correlation that exists between the nuclear $H\beta$ and 25μm luminosities (Dultzin-Hacyan et al. 1988). The "IR-loudness" α(V,60) measures the relative galactic extinction and has also been used as a warm dust indicator (Keel et al. 1994), correlating with the ratio f_{60}/f_{100}. Finally, the IR colour index IRCI, defined by Dahari & de Robertis (1988), indicates the IR colour deviation of Seyferts compared to non-active spirals. They had found it to be typically ~ 1.75 for Seyfert 1s and ~ 1.55 for Seyfert 2s.

In Table 10 we list for comparison the mean properties of three well-known samples: (i) The ultra-luminous far-IR galaxies (ULFIRGs), with $L_{FIR} \gtrsim 10^{12} L_\odot$ (Sanders et al. 1988), which appear to be associated with advanced mergers and their far-IR emission is mainly due to thermal emission, reradiated by hot dust ($\sim 50^o$K). (ii) A subsample of the Markarian galaxies (MKN), that contains on-going and advanced merging systems with mean projected nuclear separation ~ 3.5 kpc (Mazzarella et al. 1991). Their UV excess indicates starburst or Seyfert nuclear activity. (iii) A subsample of the complete IRAS Bright galaxy sample (BG), with $f_{60} \gtrsim 5.24$ Jy (Soifer et al. 1989), that was chosen by Mazzarella et al. (1991) to contain only the non-interacting members.

We find that Mkn 463 has the highest L_{FIR} luminosity that progressively decreases towards UGC 3995 (Table 9), while the total (mid-to-far) $MFIR$ flux density is comparable between the four objects. The same trend is found for the 60/100 μm flux
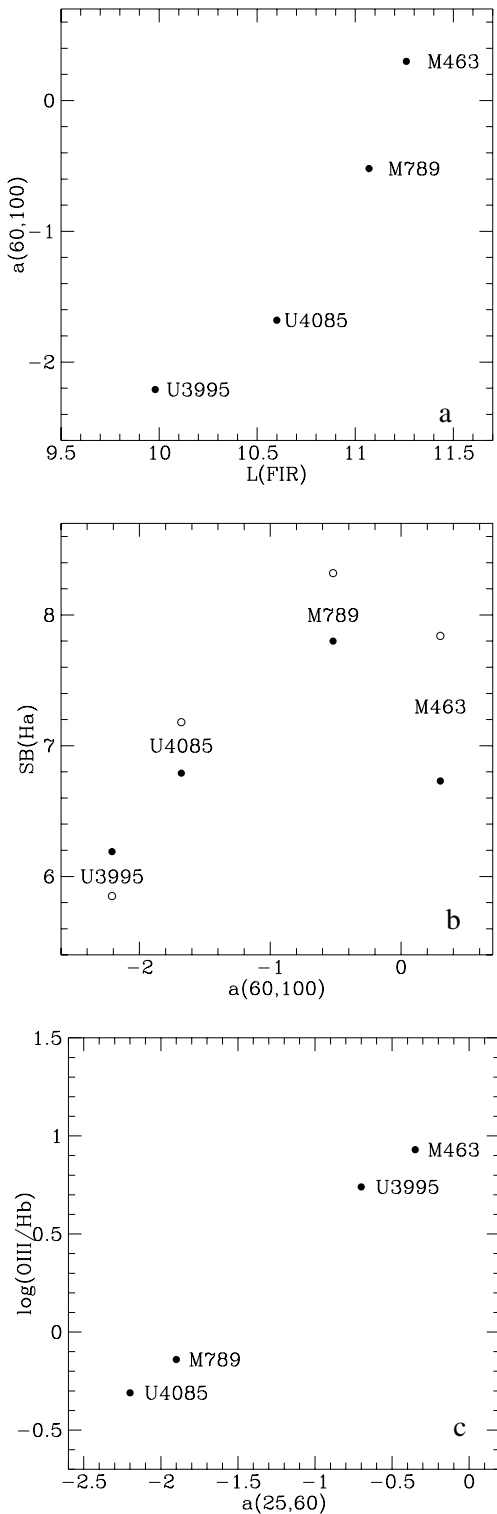
Fig. 18. a Far-IR luminosity against 60-100μm colour index, **b** 60-100μm colour index against nuclear (open symbols) and total (filled symbols) $H\alpha$ surface brightness and **c** 25-60μm colour index against the log$\frac{[OIII]_{5007}}{H_\beta}$ ratio of the brightest nucleus/hotspot, for our four objects.

ratio: for Mkn 463 the α(60,100) index is comparable (larger) to the mean value for the ULFIRG sample, for Mkn 789 is comparable to the mean for the MKN sample, while UGC 4085 and UGC 3995 have cooler colours compared to those for isolated galaxies. In Figs. 18a,b we plot the L_{FIR} vs f_{60}/f_{100} and the f_{60}/f_{100} vs $H\alpha$ surface brightness (nuclear/total are symbolized by open/filled dots, respectively). The f-IR luminosity certainly scales with warmer 60-100 μm colours and higher $H\alpha$ luminosities. The position of Mkn 463 indicates an important contribution from the AGN to both the L_{FIR} and f_{60}/f_{100}. Mazzarella et al. (1991) have indeed suggested for this object, that the IR emission is dominated by a compact source centered on the east, Seyfert 1 nucleus. In Fig. 18c we plot the α(25,60) spectral index against the log$\frac{[OIII]_{5007}}{H_\beta}$ ratio of the brightest nucleus/hotspot. The two galaxies harbouring a Seyfert nucleus, i.e., Mkn 463 and UGC 3995, have much warmer (i.e., flatter) 25 to 60 μm colours and similarly large IRCI. The AGN is obviously dominating the 25-100 μm emission in these objects.

In Fig. 19a we reproduce the colour-colour diagram of Mazzarella et al. (1991) which is based on models calculated by Xu & de Zotti (1989). Here, two effects are illustrated: the relative dominance of the warm over the cooler dust component (dotted lines) and the variation of the warm dust temperature (solid lines) along the diagram. The position of the various samples on this diagram, as produced by Mazzarella et al. (1991), show a clear progression in the warm dust component temperature and relative importance, from the isolated RSA sample (brightest optically selected normal galaxies, Sandage & Tammann 1981) ($T_d \sim 30^o$K) towards the BG ($T_d \sim 35^o$K) the MKN ($T_d \sim 40^o$K) and the ULFIRG ($T_d \sim 50^o$K) samples. We find that the dust content ($T_d \sim 30^o$K and warm/total dust $\sim 35\%$) of UGC 4085 is comparable to the mean for the RSA sample. On the other hand, Mkn 789 has a much warmer ($T_d \sim 50^o$K) dominant ($\sim 70\%$) dust component. Mkn 463 and UGC 3995 do not fit in the scheme of Fig. 19a, which was calculated for non-Seyfert Markarian galaxies (Xu & de Zotti 1989). They are both shifted towards higher 12/25 flux ratios, indicating the contribution of the AGN. It has indeed been shown that the 12-25μm spectrum of Seyferts is much less steep than that of starburst galaxies (Rowan-Robinson 1987), due to an extra component with power law spectrum between 1-10μm.

In Fig. 19b we reproduce the $log(L_{FIR})$ vs $log(L_{H\alpha+[NII]})$ diagram from Armus et al. (1990) where we show the loci for a colour-selected sample of powerful FIR galaxies (ICSS), together with those for a sample of optically selected, strongly interacting spiral galaxies (BLW) (Bushouse et al. 1988) and a sample of (optically selected) isolated spiral and irregular galaxies (KK) (Kennicutt & Kent, 1983). We also show the mean values for these samples and the positions of our four objects in this diagram.

Mkn 789 has IR luminosity and colours in the ranges defining the ICSS ($L_{FIR}=10^{10}$-$10^{12}L_\odot$, α(25,60) $\lesssim$ -1.5 and α(60, 100)$\gtrsim$ -0.5) making it directly comparable to this class of objects. Both Mkn 463 and Mkn 789 have a larger $(H\alpha + [NII])/FIR$ luminosity ratio than the mean value for the ICSS FIRGs. Their $L_{H\alpha+[NII]}$ luminosity is at the brightest
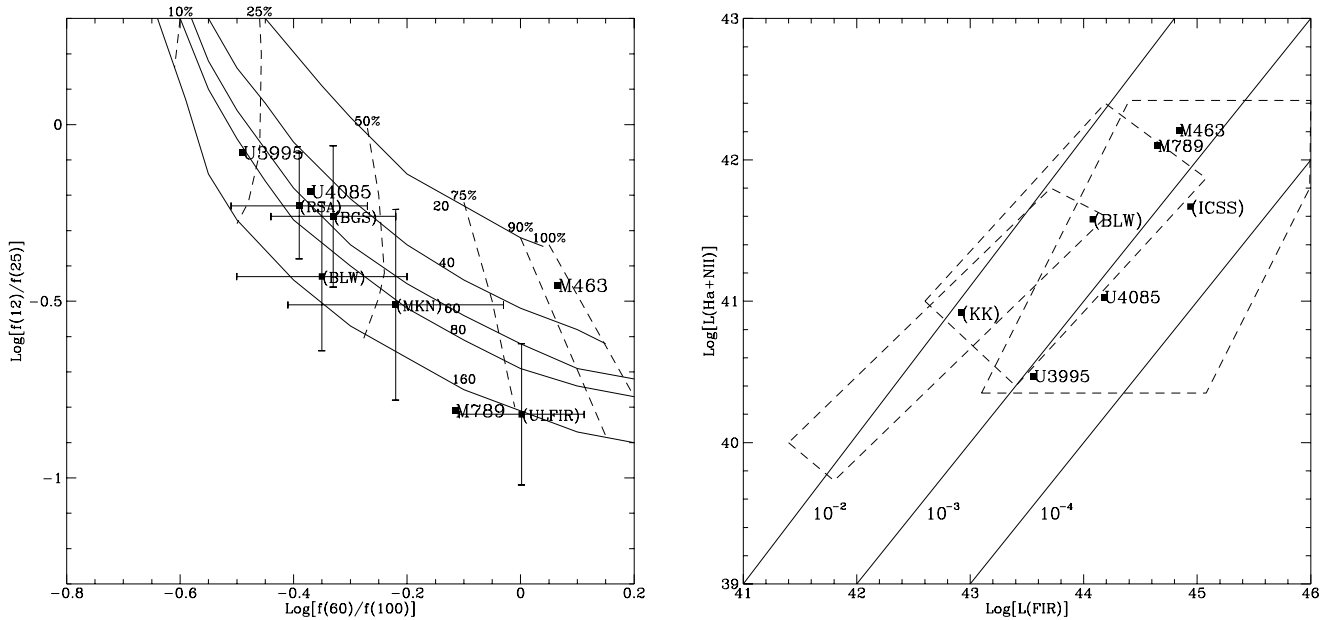
Fig. 19. a Colour-colour diagram (reproduction from Mazzarella et al. 1991), where solid curves represent selected relative intensities of the warm dust component relative to the local ISRF (i.e., a measure of dust temperature) and dashed curves represent selected ratios of the warm/warm+cold dust component (i.e., dominance of the warm over the cool dust component). All curves are model predictions from Xu & de Zotti 1989). The points represent values for the four objects of our sample (M463, M789, U4085, U3995) and mean values (with associated standard deviations) for a few selected samples (Mazzarella et al 1991): RSA (optically selected isolated galaxies, Sandage & Tammann 1981), BGS (IR bright isolated galaxies, Mazzarella et al. 1991), BLW (optically selected interacting galaxies, Bushouse et al. 1988), MKN (Markarian mergers, Mazzarella et al. 1991) and ULFIR (ultra-luminous far-IR galaxies, Sanders et al. 1988). **b** $log(L_{FIR})$ vs $log(L_{(H\alpha+[NII])})$ diagram (reproduction from Armus et al. 1990). The loci of the ICSS (Infrared Colour Selected Sample of powerful FIR galaxies, Armus et al. 1990), the BLW and the KK (optically selected isolated spiral and irregular galaxies, Kennicutt & Kent 1983) samples are plotted (dashed lines) as well as the points indicating the mean sample values and the positions of our four objects. The solid diagonal lines are the loci of selected ratios.

end of the BLW locus, indicating that the current star formation in these mergers is larger (factors 6 and 3 respectively) than the mean *total* star formation in interacting galaxy pairs. The $L_{H\alpha+[NII]}$ of UGC 4085 is similar to that of isolated spirals, but its "excess" L_{FIR} brings it inside the ICSS loci. Finally, UGC 3995 has very little line emission, while its far-IR excess must be directly related to its Seyfert nucleus (see previous paragraph). So far we have compared observed rather than intrinsic luminosities between samples/objects and, according to Armus et al. (1990), the differing internal extinction is one of the factors causing the large scatter in the above diagram. They estimate a mean extinction of 3 magnitudes in $H\alpha$ for their sample, which is similar to the correction applied for Mkn 789 and UGC 4085 but larger by ~ 1.5 magnitude than the mean extinction for Mkn 463. Consequently, our conclusions above still apply to the corrected $L_{H\alpha+[NII]}$ luminosities.

6.6. Light concentration

We have computed the mean $H\alpha+[NII]$ nuclear surface brightness for our objects and find them to be ~ 8.03, 8.1, 7.1 and 6.1 $L_\odot$/kpc^2 for Mkn 463, Mkn 789, UGC 4085 and UGC 3995 respectively, considering the sum of the two main nuclei. These numbers do not change much if we only consider the brightest nucleus/hotspot (8.02, 8, 7, 6.1 respectively). For comparison,

the mean $H\alpha + [NII]$ nuclear surface brightness for the ICSS FIRGs is ~ 7 $L_\odot$/kpc^2 (Armus et al. 1990). This might be another indication that it is the strong nuclear emission that powers the far-IR luminosity in our objects, as has been claimed to be the case for the ICSS FIRGs (Armus et al. 1990). We have also derived the % contribution of the brightest nucleus to the total $H\alpha + [NII]$ luminosity. The most compact nuclear emission is found for Mkn 789 and UGC 4085, where $\sim 30\%$ of the total line emission comes from the central 1 kpc^2 region. We can calculate in a similar way the starlight concentration, L_{Bn}/L_{Bt} and we find that the contribution of the central 1 kpc^2 region to the total blue luminosity is of the order of at most $\sim 4\%$, 24%, 18% and 6% for Mkn 463, Mkn 789, UGC 4085 and UGC 3995 respectively. Comparison of these numbers could indicate that the emission line gas is more centrally concentrated than the starlight but our total blue luminosity is measured over a larger area than the total $L_{H\alpha+[NII]}$ (covered by our spectrograph) which would precisely lead to an overestimation of the emission line gas concentration, consequently we will not attempt any conclusions here.

Last, we compare the luminosities of the individual nuclei/hotspots of our objects. For Mkn 463, the line emission $L_{H\alpha+[NII]}$ of nucleus E is 20 times larger than that of nucleus W, while the ratio of L_B luminosities is down by a factor of 10. The somewhat more even distribution of the starlight be-

tween the two nuclei indicates that, while the precursor galaxies might have been of rather similar size and stellar content, the merger has turned on the nuclear activity in the eastern component which is now the main source of ionization in this object (see also Paper I). For Mkn 789, the $L_{H\alpha+[NII]}$ luminosities of regions A and C (principal star forming regions in this object) are comparable, whereas the line emission on region B is fainter by a factor of ~ 5. Region A, the likely location of the nucleus/nuclei in this object, is also the brightest in blue light by a factor of ~ 3 compared to either B or C. For UGC 4085, knot A is bluer than B by a factor of ~ 2, while the line emission is rather evenly distributed between the two knots (factor ~ 1.3). For this object however, the L_{Bn} luminosity ratios might be affected by the variable extinction between the two knots (Sect. 4), while this is less important for the previous two objects.

6.7. Recent vs past star formation

The optical and IR luminosities measure star formation over slightly different time periods (Armus et al. 1990). $L_{H\alpha}$ is mainly due to ionization by young stars ($\lesssim 10^7$ yr) while L_{FIR} is a measure of the star formation over the past 10^8-10^9 yr. We have calculated both star formation rates (SFR) for each object and display them in Table 9:

(6a) SFR calculated from the "total" $H\alpha$ luminosity, corrected for internal extinction (line (2a)), through the relation:

$SFR_{H\alpha} = 7.07 \times 10^{-42}$ $L_{H\alpha}$ $M_\odot yr^{-1}$

adopted from Hunter & Gallagher (1986) for a Salpeter IMF between 0.1 and 100 M_o (Armus et al. 1990).

(6b) star formation rate calculated from the f-IR luminosity given in (5b), through the relation:

$SFR_{IR} = 1.3 \times 10^{-43}$ L_{FIR} $M_\odot yr^{-1}$

adopted from Hunter et al. (1986) (Armus et al. 1990).

The corresponding numbers for two of the comparison samples that we have used above are: $SFR_{H\alpha}$=40 $M_\odot yr^{-1}$ and SFR_{IR}=117 $M_\odot yr^{-1}$ for the IR colour selected FIRGs sample (ICSS, Armus et al. 1990), while $SFR_{H\alpha}$=6.79 $M_\odot yr^{-1}$ and SFR_{IR}=12.49 $M_\odot yr^{-1}$ for the Markarian mergers (MKN, Mazzarella et al. 1991). Most of the ICSS FIRGs are probably merger products (Armus et al. 1990) but they were selected to have cold IR colours, consequently large star formation rates. Mkn 789, has SFRs smaller by a factor of ~ 2 than the mean for the ICSS sample (with which is directly comparable), but larger than the typical values for Mkn mergers by factors of ~ 2 and 5 (for the $SFR_{H\alpha}$ and SFR_{IR} respectively). Its $SFR_{IR}/SFR_{H\alpha}$ ratio is ~ 3 and Armus et al. (1990) argue that this value is within the uncertainties attached to the models used for the calculation of the SFRs. This result is yet another evidence that Mkn 789 must be a *recent* merger product, undergoing strong star formation events.

Mkn 463 has a smaller current $SFR_{H\alpha}$ but the rate derived from its far-IR luminosity is comparable to that for the ICSS sample. The corresponding $SFR_{IR}/SFR_{H\alpha}$=7.4 is consistent with the result drawn previously from its IR colours, i.e. that the Seyfert nucleus is probably contributing to most of its far-IR luminosity, rather than indicating a declining star formation rate.

Table 10. Miscellaneous Properties of Comparison Samples

Properties	ULFIRGs[1]	MKN mergers[2]	BGS isolated[3]
V_{sys}(km s^{-1})	15807	8500	2250
$Log(A)$(kpc^2)	3.29	2.14	2.41
$Log(L_{Bt})(L_\odot)$	10.10	9.82	9.93
S(kpc)	(2.9)	3.5	-
$Log(L_{FIR})(L_\odot)$	11.90	10.40	10.30
$\alpha(25, 60)$	-2.35	-0.39	
$\alpha(60, 100)$	0.09	-0.99	-1.49
$\alpha(V, 60)$	-2.44	-2.24	
$SFR_{FIR}(\frac{M_\odot}{yr})$	395	12.49	9.92

The meaning of the quantities in this table is similar to those in Table 9 (see text) [1] Ultra Luminous Far-IR Galaxies (Sanders et al. 1988) [2] Advanced Markarian Mergers (Mazzarella et al. 1991) [3] Non-interacting members of the complete Bright Galaxy Sample (Soifer et al. 1989)

The same conclusion must be drawn for UGC 3995, for which the current SFR is smaller than the typical value for isolated spirals and the $SFR_{IR}/SFR_{H\alpha}$=52.

In UGC 4085, more than half of the line emission comes from bright knots in the spiral arms and its $SFR_{H\alpha}$ is rather low, comparable to isolated normal galaxies. The rather similar distribution of starlight and emission line gas in this object and its "cold" IR colours suggest the presence of a diffuse dust component, heated by the ISRF which is dominated by old stars. The large ratio of past/current SFR ~ 17 (Table 9), that we find for this object, is then more likely indicating a declining star formation rate. Alternatively, this ratio might be underestimated due to the only partially covered field to which our "total" $SFR_{H\alpha}$ is referring. This might also be the case for UGC 3995, where a large part of its spiral structure was not covered by our spectrograph. However it is less likely that it has affected the results for Mkn 789, where most of the line emission is coming from the central regions, or for Mkn 463 whose IR emission is mainly coming from a compact source centered on the east nucleus (Mazzarella et al. 1991).

7. Conclusions

We have undertaken a program of studying the central few kpc regions of galaxies in various stages of interaction/merging using three-dimensional spectroscopy. In this second paper we have presented data for three more objects and our main conclusions are:

(1) Mkn 789 has a fuzzy, irregular appearance, containing several emission regions within a common envelope and exhibiting bright extensions that resemble tidal features. SE of the main structure A, we detect double peaked emission line profiles indicating that gas is accelerated up to 600 km sec^{-1} within a region of few arcsec across (denoted by "C"). Line ratio diagnostics are consistent everywhere with gas photoionized by hot stars, the line splitting region showing the highest ionization. This one-to-one relation indicates a common mechanism

between the gas motions and the strong star formation in this object. We argue, on the basis of energetic arguments, that the starburst drives a large scale outflow ("superwind") over a period of few 10^7 yr. Mkn 789 has a large IR luminosity and warm far-IR colours, that make it directly comparable to the class of powerful FIRGs. All its observed properties suggest that it is a recent merger product, undergoing a strong burst of star formation, while the older stellar component did not have yet the time to relax. Whether any nucleus has survived is unclear, as it could well be obscured by the large amounts of dust that reside in the central regions and/or confused with the intense "central" starburst.

(2) UGC 4085 exhibits a knotty spiral structure and two giant emission knots in the central 3 kpc. Both are elongated and have low ionization spectra, characteristic of HII regions. Knot B (the faintest optically) maybe indicates the location of the galactic nucleus that remains embedded in large amounts of dust. However, there is no real evidence for it to be a merger. Its velocity field resembles a smoothly rotating disk, with knot B close to the kinematic center. We find a declining star formation rate and the emission line luminosity and distribution are comparable to those of normal spiral galaxies. UGC 4085 has a rather high IR luminosity, but its IR colours indicate the dominance of a cold dust component, similar to that in isolated galaxies.

(3) UGC 3995 is the brightest member of a pair of interacting spirals. Line emission has been detected in the central 1 kpc region, showing a low-ionization Seyfert-like spectrum. The velocity field is characteristic of a smoothly rotating disk, but we find rotation of the kinematic axis as defined by different emission lines, that correspond to isophotal distortions. The highly ionized gas ($[OIII]$) has an extended morphology that coincides with a bar-like structure seen in starlight. Substructure in the $[OIII]_{5007}$ line profiles is interpreted as additional velocity components possibly indicating gas inflow along the bar. It is important to confirm that with higher spatial and spectral resolution data. UGC 3995 does not show excess L_{FIR} but does have very warm mid-IR colours, suggesting that the AGN must be providing the main dust heating mechanism.

(4) The large IR activity, as expressed by the L_{FIR} excess and "warm" far-IR colours, of the two advanced mergers presented so far Mkn 789 and Mkn 463 (Paper I), seems to be independent of the nature of their central engine (AGN and starburst respectively). In an analogous way, the 25 μm excess emission of the Seyfert nuclei in Mkn 463 and UGC 3995, seems to be independent of the nature, interaction stage or far-IR properties of the host galaxy.

(5) Unraveling the gas dynamics due to the merging is a very difficult task. The superwind in Mkn 789, the ionization cone in Mkn 463 (and possibly in UGC 3995) and the coupling between the radio jet and the ambient gas in Mkn 463, indicate that hydrodynamic processes are probably dominating the kinematics in the central 10-20 kpc regions of these systems. On the other hand, the absence of an appreciable general velocity gradient in Mkn 789 and Mkn 463 might be a direct result of strong tidal forces that have been exerted on these systems, annihilating any strong signs of rotational motion in the parent galaxies.

8. Future work

Naturally, our approach does not provide a unique description of the merger of two disk galaxies. The properties of the progenitors and the encounter initial conditions are two decisive factors that influence the evolution of the systems through the various stages of the interaction and these cannot be provided by our data. The multiplicity of factors that can influence the observable characteristics of an advanced merger, make it very difficult to fit our objects in a common sequence of events. In order to improve our understanding of a possible evolutionary connection between starburst and AGN activity and how this relates to the merging process, we need to complete this sequence with more objects from our observed sample and repeat the above lines of thinking. In a third paper we will present data for four additional intermediate-stage interactors:

(1) Mkn 176, a complicated interacting system involving three galaxies, whose disks suffer tidal distortions. We have detailed spectroscopic data for all three members and at least one of them harbours a Seyfert nucleus.

(2) IRAS 13144+4508, a member of a disk-disk encounter where both galaxies exhibit tidal tails. It also harbours a Seyfert nucleus.

(3) IRAS 09406+1018, a disk galaxy strongly interacting with at least two smaller companions. Tidal features are emanating from the group. This is most probably a starburst galaxy.

(4) Mkn 373, a Seyfert galaxy that appears to be a normal spiral, with a companion (advanced merger) galaxy, visible at $\sim$ 44 kpc projected distance. Mkn 373 will be used as a "template" Seyfert galaxy if the detailed kinematic study shows it to be a "normal" spiral galaxy.

The distribution and amount of atomic and molecular gas in these objects are necessary pieces of information in order to understand the mechanisms through which fuelling of the central engine occurs. Moreover, IR imaging at sufficiently large wavelengths is necessary, in order to penetrate the dusty central regions and detect any remaining non-stellar nuclei.

References

Armus, L., Heckman, T.M., Miley, G.K. 1990, ApJ 364, 471
Amram, P., Boulesteix, J., Marcelin, M., Balkowski, C., Cayatte, V., Sullivan, W.T., III 1995, A&AS 113, 35
Barnes, J.E., Hernquist, L.E. 1996, ApJ 471, 115
Bernloehr, K. 1992, A&A 263, 54
Bernloehr, K. 1993, A&A 268, 25
Bica, E., Alloin, D. 1986, A&A 166, 83

Bica, E., Alloin, D., Schmidt, A. 1990, MNRAS 242, 241

Binette, L., Dopita, M.A., Tuohy, I.R. 1985, ApJ 297, 476

Bothun, G.D., Aaronson, M., Schommer, B., Mould, J., Huchra, J., Sullivan, W.T. ApJS 57, 423

Bottinelli, L., Gouguenheim, L., Paturel, G., De Vaucouleurs, G. 1983, A&A 118, 4

Bottinelli, L., Gouguenheim, L., Fouque, P., Paturel, G., 1990 A&AS 82, 391

Bushouse, H.A., Werner, M.W., Lamb, S.A. 1988, ApJ 335, 74

Chatzichristou, E.T., Vanderriest, C. 1995, A&A 298, 343 (Paper I)

Chevalier, R.A., Clegg, A.W. 1985, Nature 317, 44

Christian, C.A., Adams, M., Barnes, J.V., et al., 1985, PASP 97, 363

Cutri, R.M., Mc Alary, C.W. 1985, ApJ 296, 90

Dahari, O., De Robertis, M.M. 1988, ApJS 67, 249

Davis, L.E., Seaquist, E.R. 1983, ApJS 53, 269

De Grijp, M.H.K., Lub, J., Miley, G.K. 1987, A&AS 70, 95

De Grijp, M.H.K., Keel, W.C., Miley, G.K., Goudfrooij, P., Lub, J., 1992, A&AS 96, 389

Dopita, M.A., Sutherland, R.S. 1995a, ApJ 455, 468

Dopita, M.A., Sutherland, R.S. 1995b, ApJS 102, 161

Dultzin-Hacyan, D., Masegosa, J., Moles, M. 1990, A&A 238, 28

Dultzin-Hacyan, D., Moles, M., Masegosa, J. 1988, A&A 206, 95

Gorjian, V. 1995, ApJ 450, L51

Heckman, T.M., Armus, L., Miley, G.K. 1990, ApJS 74, 833

Heckman, T.M., Lehnert, M.D., Armus, L. 1993, in "The Environment & Evolution of Galaxies", eds. J. M. Shull and H. A. Thronson, Jr. (Dordrecht: Kluwer), p. 455

Helou, G., Khan, I.R., Malek, L., Boehmer, L. 1988, ApJS 68, 151

Heyl, J.S., Hernquist, L.E., Spergel, D.N. 1996, ApJ 463, 69

Hibbard, J.E., Van Gorkom, J.H. 1996, AJ 111, 655

Hodge, P., Lee, M.G., Kennicutt, R.C. 1989, PASP 101, 32

Hodge, P., Miller, B.W. 1995, ApJ 451, 176

Hunter, D.A., Gallagher, J.S., III 1986, PASP 98, 1099

Hunter, D.A., Gillett, F.C., Gallagher, J.S., Rice, W.L., Low, F.J. 1986, ApJ 303, 171

Karachentsev, I.D. 1972, Soobshch. Spets. Astrof. Obs. 7, 1

Keel, W.C. 1985, AJ 90, 2207

Keel, W.C. 1993, AJ 106, 1771

Keel, W.C., De Grijp, M.H.K., Miley, G.K., Zheng, W. 1994, A&A 283, 791

Kennicutt, R.C., kent, S.M. 1983, AJ 88, 1094

Kukula, M.J., Pedlar, A., Baum, S., O'Dea.C.P. 1995, MNRAS 276, 1262

Lamb, S.A., Gerber, R.A., Balsara, D.S. 1994, Ap&SS 216, 337

Landolt, A., 1983, AJ 88, 439

Leitherer, C., Heckman, T.M. 1995, ApJS 96, 9

Lehnert, M.D., Heckman, T.M. 1996, ApJ 462, 651

Martin, J.M., Bottinelli, L., Gouguenheim, L., Dennefeld, M. 1991, A&A 245, 393

Lonsdale, C.J., Helou, G., Good, J.C., Rice, W. 1985, in "Catalogued Galaxies and Quasars Observed in the IRAS Survey" (Pasadena:JPL)

Mazzarella, J.M., Boroson, T.A., 1993, ApJS 85, 27

Mazzarella, J.M., Bothun, G.D., Boroson, T.A. 1991, AJ 101, 2034

Michel, A., Huchra, J. 1988, PASP 100, 1423

Mihos, J.C., Hernquist, L. 1994, ApJ 431, L9

Mihos, J.C., Hernquist, L. 1996, apJ 464, 641

Miley, G.K., De Grijp, M.H.K. 1985, in "Light on dark matter" p.471, Proceedings of the First IRAS Conference Nordwijk, Netherlands, June 10-14

Osterbrock, D.E., Martel, A. 1993, ApJ 414, 5520

Penston, M.V., Fosbury, R.A.E. 1978, MNRAS 183, 479

Quillen, A.C., Frogel, Jay A., Kenney, Jeffrey D.P., Pogge, R.W., Depoy, D.L. 1995, ApJ 441, 549

Rieke, G.H., Lebofsky, M.J., Thompson, R.I., Low, F.J.,

Rozyczka, M. 1985, A&A 143, 59

Tokunaga, A.T. 1980, ApJ 238, 24

Rowan-Robinson, M. 1987 in "Star Formation in Galaxies", p 133, NASA, Washington

Sandage, A., Tammann, G.A. 1981, "A Revised Shapely-Ames Catalogue of Bright Galaxies", Carnegie Institution of Washington

Sanders, D.B. 1992, in "Relationship between AGN and Starburst Galaxies", ed.T.Lee

Sanders, D.B., Soifer, B.T., Elias, J.H., Madore, B.F., Matthews, K., Neugebauer, G., Scoville, N.Z. 1988, ApJ 325, 74

Schweizer, F. 1996, AJ 111, 109S

Soifer, B.T., Boehmer, G., Neugebauer, G., Sanders, D.B. 1989, AJ 98, 766

Surace, J.A., Mazzarella, J., Soifer, B.T., Wehrle, A.E. 1993, AJ 105, 864

Suchkov, A.A., Balsara, D.S., Heckman, T.M., Leitherer, C. 1994, ApJ 430, 511

Suchkov, A.A., Berman, V.G., Balsara, D.S., Heckman, T.M. 1996, ApJ 463, 528

Telesco, C.M., Wolstencroft, R.D., Done, C 1988, ApJ 329, 174

Tomisaka, K., Ikeuchi, S. 1988, ApJ 330, 695

Vanderriest, C. 1993, ASP Conf.Ser. 37, 338

Vanderriest, C., Lemonnier, J.P. 1988, in "Instrumentation for Ground-based Optical Astronomy", Proc. IX Santa Cruz Workshop, p.304

Veilleux, S., Osterbrock, D.E. 1987, ApJS 63, 295

Veron-Cetty, M.-P., Veron, P. 1986, A&AS 65, 241

Wilson, A.S. 1996, Vistas in Astronomy 40, p.63

Wilson, A.S., Tsvetanov, Z.I. 1994, AJ 107, 1227

Xu, C., De Zotti, G. 1989, A&A 225, 12